ISPRS Journal of Photogrammetry and Remote Sensing 196 (2023) 429–444

Contents lists available at ScienceDirect

ISPRS Journal of Photogrammetry and Remote Sensing

journal homepage: www.elsevier.com/locate/isprsjprs

Tracking changes in coastal land cover in the Yellow Sea, East Asia, using Sentinel-1 and Sentinel-2 time-series images and Google Earth Engine

Yongchao Liu [a,b], Xiangming Xiao [b,*], Jialin Li [a,*], Xinxin Wang [c], Bangqian Chen [d], Chao Sun [a], Jie Wang [e], Peng Tian [a], Haitao Zhang [a]

[a] *Department of Geography and Spatial Information Techniques, Donghai Academy, Ningbo Universities Collaborative Innovation Center for Land and Marine Spatial Utilization and Governance Research, Ningbo University, Ningbo 315211, China*
[b] *Department of Microbiology and Plant Biology, Center for Earth Observation and Modeling, University of Oklahoma, Norman, OK 73019, USA*
[c] *Ministry of Education Key Laboratory for Biodiversity Science and Ecological Engineering, National Observations and Research Station for Wetland Ecosystems of the Yangtze Estuary, Institute of Biodiversity Science and Institute of Eco-Chongming, School of Life Sciences, Fudan University, Shanghai 200438, China*
[d] *Rubber Research Institute, Chinese Academy of Tropical Agricultural Sciences, Hainan 571737, China*
[e] *College of Grassland Science and Technology, China Agricultural University, Beijing 100094, China*

A R T I C L E I N F O

Keywords:
Coastal land cover
Rule-based Time Series Classification algorithm
Sentinel-1/2 images
GEE
Yellow Sea

A B S T R A C T

Coastal zones are essential ecosystems due to their provision of invaluable ecosystem services. However, the geomorphologic characteristics of coastal zones are becoming more complex and changeable due to global warming, sea-level rise (SLR), and the intensification of anthropogenic activities. Therefore, accurate and timely knowledge of coastal land cover types (including tidal flats, coastal vegetation, and year-long water cover) is needed for coastal research and sustainable management. To date, land cover products for coastal areas are mainly derived from moderate resolution imaging spectroradiometer images, but few studies have used Sentinel-1 synthetic aperture radar (S1) and Sentinel-2 Multispectral Instrument (S2) images, which can provide more detailed maps. We developed a Rule-based Time Series Classification (RTSC) approach to map coastal land cover types at a 10 m resolution, combining S1/S2 time-series images (2015–2019) and Google Earth Engine (GEE). These products were developed for the coastal zone of the Yellow Sea (YS), East Asia, which is an essential ecosystem protecting a coastal population of 60 million people from storms and SLR effects. Accuracy assessment showed that the annual maps of coastal land cover had high overall accuracy. The coastal land cover types for the YS in 2019 comprised 3593.42 km^2 of tidal flats, 28,506.98 km^2 of coastal vegetation, and 5436.92 km^2 of coastal year-long water. The interannual dynamics of the coastal land cover area in the YS during 2015–2019 were smaller. This study provides a promising method that combines S1/2 time series, a RTSC approach, and GEE to map coastal land cover areas at large scales. The 10 m resolution maps generated in this study are the most current dataset of coastal land cover types for the YS, and they potentially provide a basis for the sustainable management and conservation of this important coastal zone.

1. Introduction

The coastal zone is the interface between terrestrial and marine ecosystems (Adger et al., 2005; Mentaschi et al., 2018). It provides essential habitats for wildlife fauna and flora, acts as a carbon sink (Bauer et al., 2013; Pendleton et al., 2012), and suppors the sustainable development of coastal communities. However, coastal geomorphologic processes at a global scale are becoming more complex, sensitive, and changeable as a result of climate change and anthropogenic activities (Jevrejeva et al., 2016; Schuerch et al., 2018; Wang et al., 2020a). According to the coastal ecosystem investigations (Murray et al., 2014; Sun et al., 2017; Yim et al., 2018; Liu et al., 2018; Chen et al., 2019), loss of coastal wetlands is mainly caused by direct conversion to cropland and aquaculture ponds (Kirwan and Megonigal, 2013). Therefore, this study

* Corresponding authors at: Department of Microbiology and Plant Biology, Center for Earth Observation and Modeling, University of Oklahoma, 101 David L. Boren Blvd, Norman, OK 73019, USA (X.X.); Department of Geography and Spatial Information Techniques, Ningbo University, 818 Fenghua Avenue, Jiangbei District, Ningbo, Zhejiang 315211, China (J.L.).

E-mail addresses: liuyongchao@nbu.edu.cn (Y. Liu), xiangming.xiao@ou.edu (X. Xiao), lijialin@nbu.edu.cn (J. Li), xxwang18@fudan.edu.cn (X. Wang), chbq40@163.com (B. Chen), sunchao@nbu.edu.cn (C. Sun), jiewang178@cau.edu.cn (J. Wang), tianpeng@nbu.edu.cn (P. Tian), 2011073029@nbu.edu.cn (H. Zhang).

https://doi.org/10.1016/j.isprsjprs.2022.12.029
Received 31 May 2022; Received in revised form 23 December 2022; Accepted 29 December 2022
Available online 20 January 2023

accurate annual maps of land cover, which includes coastal vegetation (e.g., cropland, saltmarshes, and mangrove forest), tidal flats (also commonly known as intertidal flats or coastal non-vegetated areas), and year-long water (e.g., aquaculture ponds and rivers) (Fig. 1), are essential and necessary for future coastal sustainability.

Fieldwork is a routine method for tracking and mapping coastal land cover. However, their unacceptable costs in terms of time and effort restrict their use over long periods and on a large spatial scale (Choi et al., 2014; Wang et al., 2019). In practice, satellite remote sensing (RS) has been increasingly considered as an important tool for providing regular observations of land cover dynamics (Gong et al., 2019). Over the past half-century, several studies generated coastal land cover maps at different spatial scales using diverse RS images (Table1), including 1 km (Bartholomé and Belward, 2005), 500 m (Friedl et al., 2010), 300 m (Arino et al., 2008), 30 m (Gong et al., 2013), and 10 m (Gong et al., 2019). However, these maps may not meet the requirements of coastal zone management given that these maps do not include coastal land cover heterogeneity. As a result, several studies provided mapped thematic products for single features such as salt marshes (Sun et al., 2021) and tidal flats (Murray et al., 2019; Jia et al., 2021). However, these products either have a relatively coarse time resolution, or they provide a few years, which is problematic for monitoring this highly dynamic and complex system, which requires an overall perspective.

Although there are many previous studies of the coastal land cover (Bhargava et al., 2020; Zhang et al., 2020), their maps seldom clearly differentiate tidal flats, vegetation, and year-long water at the coastal zone. Recently, Chen et al. (2020) revealed the changes of *Spartina alterniflora* in the Yellow River delta during the period of 2012–2019 using Worldview-2 (0.5 m), GF-1 (2 m), GF-2 (1 m), and GF-6 (2 m) data. Although very high spatial resolution data have been used to generate more detailed maps, several omission errors may exist in large-scale applications. The challenges for RS applications in the YS coastal zone are compounded by issues of frequent cloud cover, phenology with a focus on coastal vegetation, and the problem of consistent land cover identification in a mixed wave-tide environment. However, time series classification algorithms can provide classification rules based on the analysis of the vegetation life cycle (Xiao et al., 2005), which has considerable advantages in land cover mapping other years across a large scale.

Since 2015 the S2 mission has provided an unprecedented quantity of publicly available data. Many recent reports showed the usefulness of S2 images for coastal land cover mapping (Bergsma et al., 2020; Jia et al., 2021; Tassi and Gil, 2020; Tian et al., 2020). The corresponding relatively high spatial resolution and observation frequency can help in the mapping of these fragmented areas. However, some of the extracted features using S2 may contain errors due to the tidal conditions at the time of image acquisition (Zhu et al., 2019), or the omission of seasonal characteristics (Sun et al., 2021). Therefore, more research is needed to produce accurate, detailed, and updated coastal land cover maps in the YS. SAR sensors, which are independent of clouds and day/nighttime, have an improved capability for capturing vegetation structures and surface water in coastal zones (Ottinger et al., 2017; La et al., 2017). The combination of microwave and optical imagery is expected to provide complementary information. Preliminary applications have been made in the areas of near-daily river discharge (Brombacher et al., 2020), mangrove forest (Chen et al., 2017), intertidal topography (Salameh et al., 2020), and agricultural ponds (Prasad et al., 2019). Despite these studies, however, the potential for the synergistic combination of radar and optical imagery to improve coastal land cover mapping at a large scale remains unknown.

Therefore, the objectives of this study were to (1) develop a basic approach that combines S1/2 images to map coastal land cover at a 10 m resolution; (2) apply the Rule-based Time Series Classification (RTSC) approach to evaluate the dynamics of coastal land cover; and (3) generate maps of the coastal land cover of the YS from 2015 to 2019.

2. Study area and dataset

2.1. Study area

The YS is located in the Western Pacific Ocean (32°–40°N, 120°–127°E) between three countries: China, North Korea, and South

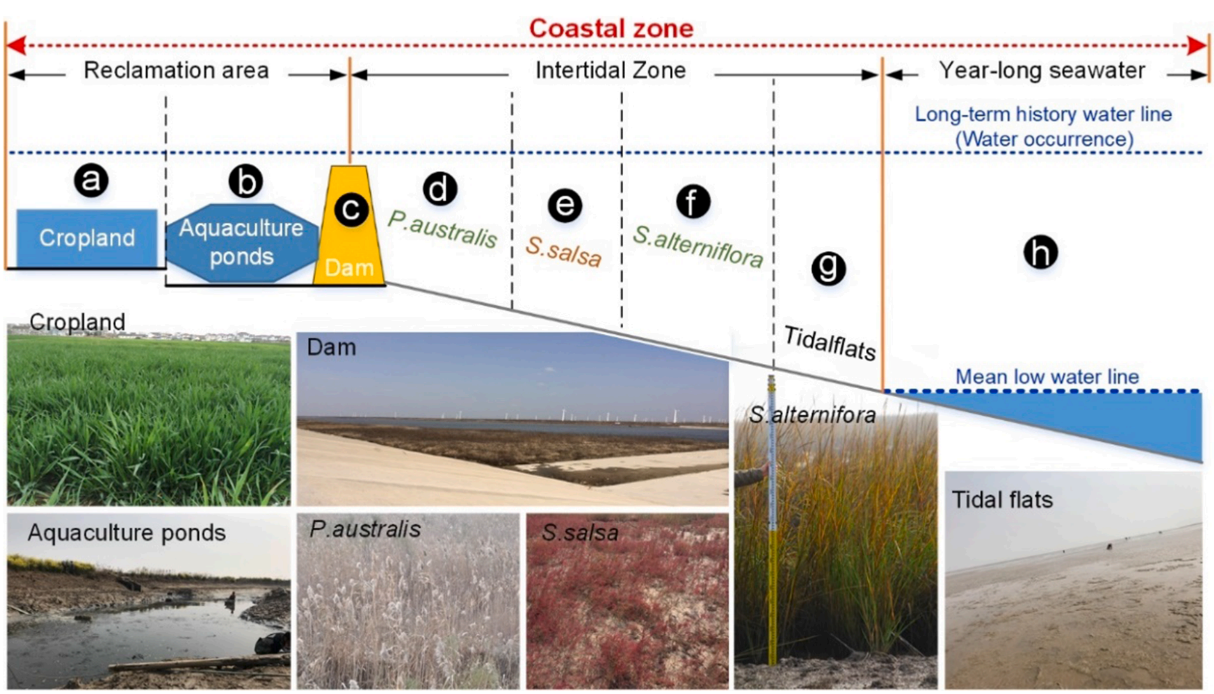

Fig. 1. Typical coastal land cover types in the Yellow Sea (YS). (a–c) cropland, aquaculture ponds, and a dam in the reclamation area, (d–g) *P. australis*, *S. salsa*, *S. alterniflora*, and tidal flats, (h) year-long seawater. (For interpretation of the references to colour in this figure legend, the reader is referred to the web version of this article.)

Table 1
Previous studies on coastal land cover mapping, including algorithms and datasets with varying spatial resolution.

Methods	Optical data			Radar data	Optical + Radar data S1/2 (10 m)
	≤10 m(e.g., S2; worldview-2; GF)	30 m(e.g., Landsat, SPOT)	250 m–500 m (e.g., MODIS)		
Visual image interpretation	Ma et al. (2019)	Niu et al. (2012), Han et al. (2019)	Bartholomé and Belward (2005)		
Unsupervised classification	Gong et al. (2019); Jia et al., (2021); Sun et al., (2021)	Amani et al. (2018), Murray et al. (2019), Zhang et al. (2019),	Bontemps et al. (2010), Bansal et al. (2017)	Mohammadimanesh et al. (2018),	
Supervised classification	Seto and fragkias. (2007); Feng et al. (2019); Chen et al. (2020)	Nielsen et al. (2008), Gong et al. (2013)	Friedl et al. (2010)		Held et al. (2003)
Pixel and time-series statistics-based methods			Wang et al. (2020a,b)		This study

Korea (Fig. 2). The YS is an essential part of a broader regional ecosystem in East Asia (Murray et al., 2014), and protects the coastal population from storms and SLR (Small and Nicholls, 2003). The region as a maritime monsoon climate, with a mean air temperature from 14 °C to 20 °C and annual precipitation from 1000 mm to 1200 mm. Between May and July, the sea surface temperature increases from 10 °C to 28 °C. The Bohai Sea, located in the northern part of the YS, includes the bays of Liaodong, Bohai, and Laizhou (Koh and Khim, 2014). These bays are one of the main way stations along the East Asian-Australasian Flyway for hundreds of thousands of migratory waterbirds species (Murray

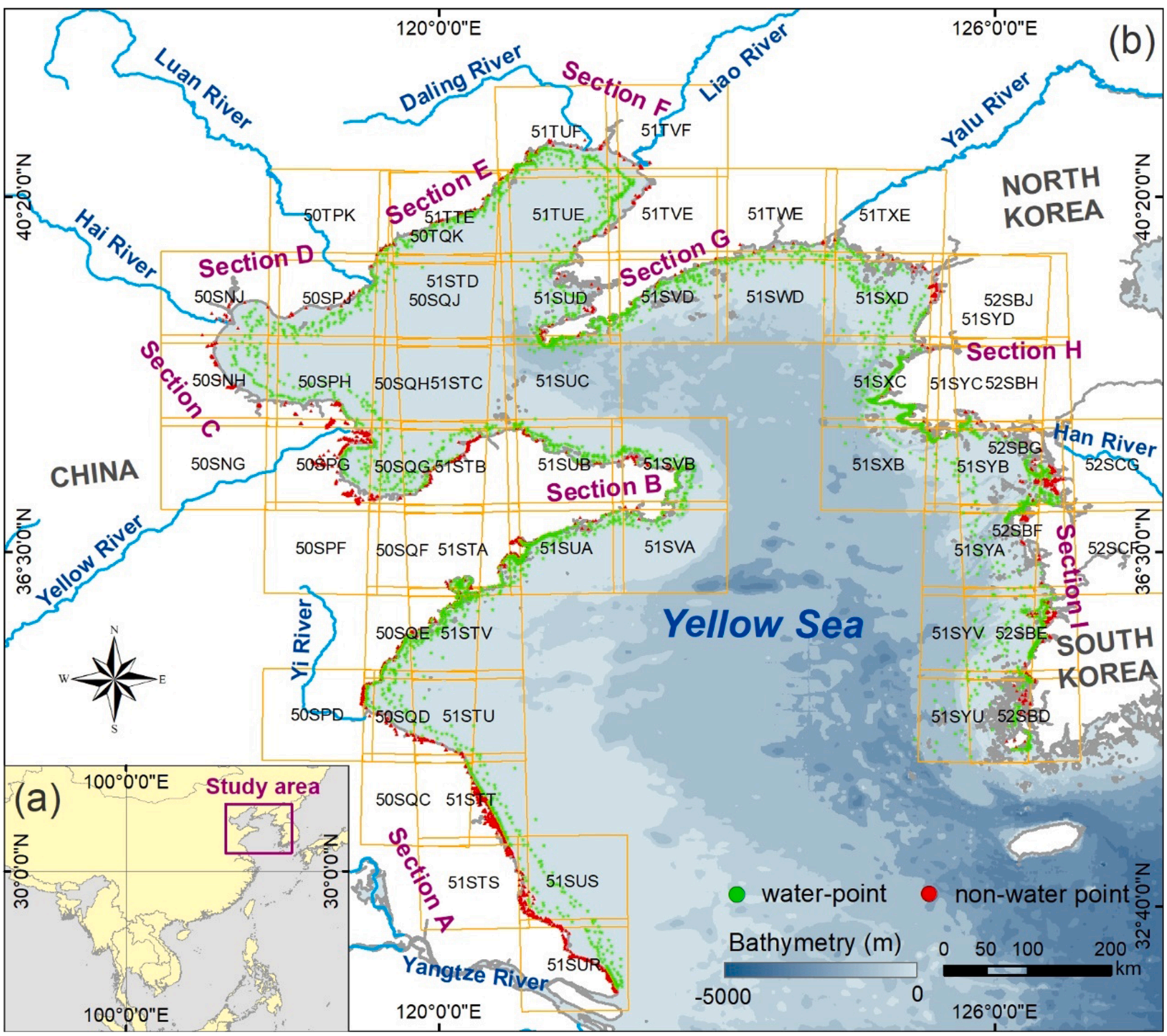

Fig. 2. (a) Map showing the location of the YS in the coastal zone of East Asia (b) Distribution of water and non-water sampling points for algorithm development. River data (i.e., primary, and secondary rivers) are from the Center for Geographic Analysis at Harvard University (available at https://worldmap.harvard.edu/).

et al., 2014). In this study, river data were used to divide the study area into nine sections (i.e., Fig. 2, A–I) to improve calculation efficiency and statistical analysis of the results.

2.2. Datasets

2.2.1. Sentinel-1 SAR and Sentinel-2 MSI images

Sentinel-1A/B satellites carry onboard a C-band synthetic aperture radar instrument that operates at 5.405 GHz, four different modes, and a revisit cycle of 12 days at the equator. S1 images acquired in ascending and descending orbits between January 1, 2015 and December 31, 2019, were selected (Fig. 3a) in GEE. The ESA Sentinel-1 observation strategy defines the Interferometric Wide swath model, which has provided dual-polarization (VV and VH) imagery. Each tile has high geometric accuracy and was generated with the Sentinel-1 Toolbox (Mahdianpari et al., 2019).

Sentinel-2A/B are a wide-swath, high spatial resolution, multi-spectral imaging mission. The S2 Level 1C images used were generated from the European Space Agency's Sentinel Scientific Data Hub. All S2 images collected by the study were processed into the atmospherically-corrected surface reflectance from the sensors. The S2 images are from June 23, 2015, to December 31, 2019. With the assistance of Quality Assessment (QA) bands, good quality observations of S2 images covering the YS coastal zone were obtained (Fig. 3b). In this study, we acquired and pre-processed all the S2 images with good quality from GEE for the interval of 2015–2019.

2.2.2. Training datasets for algorithm development

The training datasets of coastal water and non-water for algorithm development were manually and randomly identified using Google Earth images. Additionally, fieldwork photos from the Global Geo-referenced Field Photos Library at the University of Oklahoma (Xiao et al., 2011), were also included. Finally, a set of 6025 sampling points was used for algorithm development, including a number of 3420 water and 2605 non-water points (Fig. 2). Besides the abovementioned water and non-water sampling points, 12 regions of interest (ROI), of comparatively large size, were taken as training data to analyze the signatures of non-water and water areas in S1/2 images (Fig. S1). The 10 non-water ROIs included: 8 ROIs representing different types of coastal vegetation such as cropland (ID = #1 and #2), saltmarsh (ID = #3, #4, and #5), and forest (ID = #6, #7 and #8), and 2 ROIs representing tidal flats (ID = #9 and #10). Two ROIs were also selected in seawater areas with different turbidity conditions: low turbidity (ID = #11) and high turbidity (ID = #12) (Fig. S1 for ID reference).

3. Algorithms for coastal land cover mapping

We developed a Rule-based Time Series Classification (RTSC)

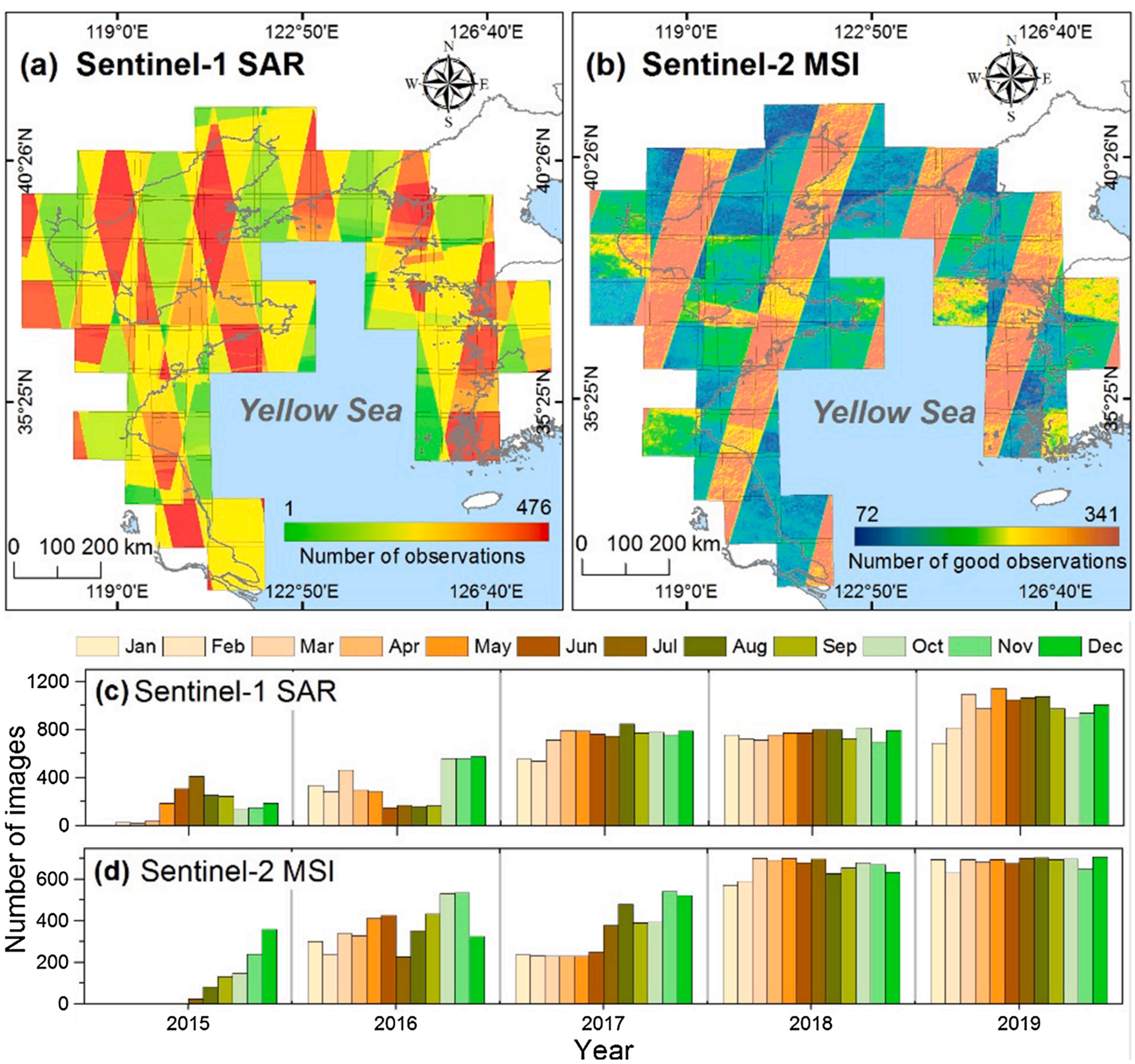

Fig. 3. S1/2 images covering the YS coastal zone. (a) The number of observations in S1. (b) The number of good observations in S2. (c–d) Monthly images collected by S1/S2 included in this study.

algorithm to classify coastal vegetation, tidal flats, and year-long water using S1/2 images, as shown in the workflow chart. The workflow was divided into three steps (Fig. 4): (a) input data, (b) classification, and (c) validation and comparison.

3.1. Extraction of surface water and vegetation

In order to perform per-pixel detection of the surface water and vegetation, several spectral indices were first calculated in the GEE. These indices were: Nominalized Difference Vegetation Index (NDVI, Tucker, 1979) (Eq. (1)), Enhanced Vegetation Index (EVI, Huete et al., 2002) (Eq. (2)), Land Surface Water Index (LSWI, Xiao et al., 2005) (Eq. (3)), and modified Normalized Difference Water Index (mNDWI, Xu, 2006) (Eq. (4)). These indices are correlated with vegetation greenness (NDVI, EVI), vegetation water (LSWI), and open surface water (mNDWI), respectively.

$$\mathrm{NDVI} = \frac{\rho_{\mathrm{NIR}} - \rho_{\mathrm{Red}}}{\rho_{\mathrm{NIR}} + \rho_{\mathrm{Red}}} \tag{1}$$

$$\mathrm{EVI} = 2.5 \times \frac{\rho_{\mathrm{NIR}} - \rho_{\mathrm{Red}}}{\rho_{\mathrm{NIR}} + 6 \times \rho_{\mathrm{Red}} - 7.5 \times \rho_{\mathrm{Blue}} + 1} \tag{2}$$

$$\mathrm{LSWI} = \frac{\rho_{\mathrm{NIR}} - \rho_{\mathrm{SWIR1}}}{\rho_{\mathrm{NIR}} + \rho_{\mathrm{SWIR1}}} \tag{3}$$

$$\mathrm{mNDWI} = \frac{\rho_{\mathrm{Green}} - \rho_{\mathrm{SWIR1}}}{\rho_{\mathrm{Green}} + \rho_{\mathrm{SWIR1}}} \tag{4}$$

Here, $\rho_{\mathrm{Blue}}, \rho_{\mathrm{Green}}, \rho_{\mathrm{Red}}, \rho_{\mathrm{NIR}}$ and ρ_{SWIR1} denote the blue band (458–523 nm), green band (543–578 nm), red band (650–680 nm), near-infrared band (ρ_{NIR}, 785–900 nm), and short-wave infrared band (ρ_{SWIR1}, 1565–1655 nm) of S2 imagery.

Although mNDWI is widely used as a standard for detecting surface water (Xu, 2006; Rokni et al., 2014), it may have errors due to the mixed pixels of water bodies and other coverage (e.g., mudflats and vegetation), especially in the coastal zone. For this reason, we used a combination of mNDWI and vegetation indices to detect surface water, which was successfully applied to Landsat images time series. Based on the randomly samples points and distribution frequency of water and non-water category are shown in Fig. 5(a–e) and our previous experimental results (Wang et al., 2021; Zou et al., 2017; Liu et al., 2020), we considered the features of NDVI, EVI, mNDWI, and LSWI from S2 images for the major coastal land cover types (Fig. S2), and VH images from S1 for water and non-water. We generated coastal land cover maps of surface water bodies and vegetation. The mapping algorithms are described below and summarized in Table 2. However, water inundation signals in the coastal zone are directly linked to the combined and highly variable effects of rivers, wind, waves, and tides. S1 data are very responsive to non-water cover (e.g., cropland, saltmarsh, and lowland forest) and water (Veloso et al., 2017). Despite some lands cover types such as beaches and mudflats (Fig. S3), the threshold VH < -28 for the S1 VH data could readily identify water (Fig. 5f). Therefore, we generated a surface water mask using the combined algorithm of [(mNDWI $>$ EVI) or (mNDWI $>$ NDVI) and (EVI $<$ 0.1) and (VH < -28)]. This method also demonstrates that S1/2 image time series have substantial advantages in coastal zone mapping (see Section 3.1 for more details).

Coastal vegetation (e.g., lowland forest, saltmarsh, and cropland) is composed of green plants with high EVI and NDVI values, which are used to detect vegetation changes throughout the year (Huete et al., 2002). However, these indices are affected by water and soil within the pixels (Wang et al., 2020b). LSWI can be used to classify vegetation and exclude surface water (Xiao et al., 2004). In our previous studies, this algorithm [(EVI $\geq$ 0.1 and NDVI $\geq$ 0.2) and LSWI $>$ 0] has been applied to MODIS (Xiao et al., 2009) and Landsat-5/7/8 (Liu et al., 2020; Wang et al., 2020b) data for vegetation mapping. Here, we also used this method to produce a coastal vegetation map among the coastal land cover types on the YS.

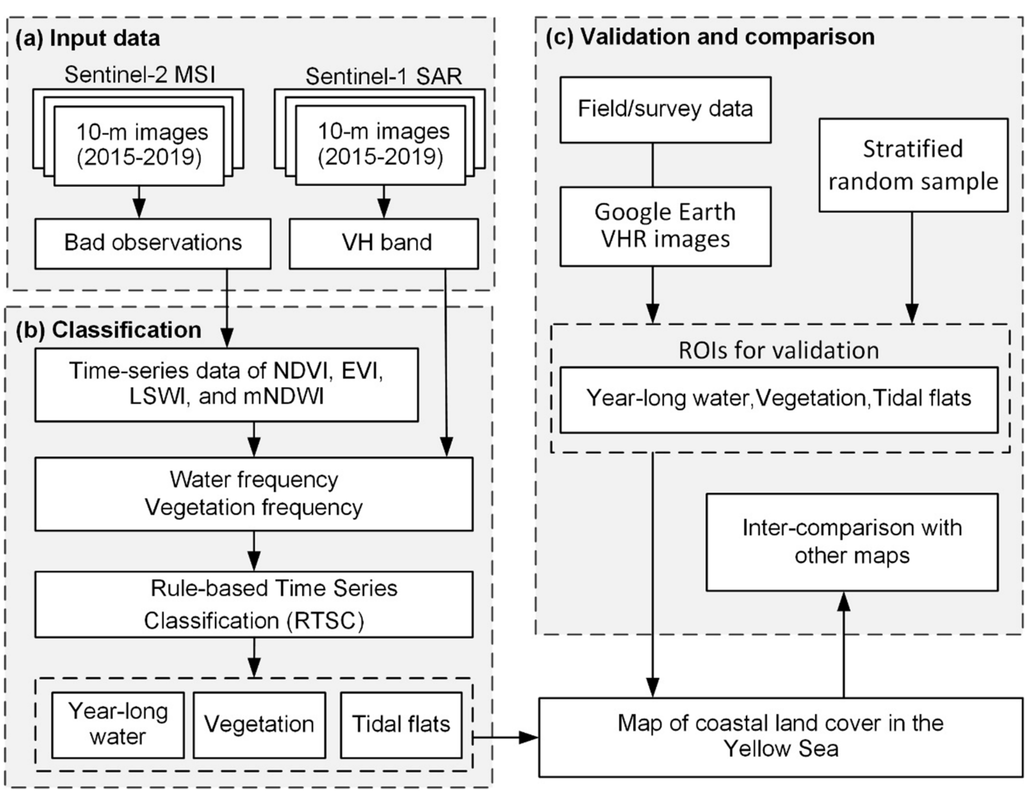

Fig. 4. Workflow chart showing the different steps in the application of the RTSC algorithm. (a) Input of S1/2 time-series data, (b) Classification of the target coastal land cover types, (c) Validation and comparison using field data and Google Earth VHR images. See the text for detailed information.

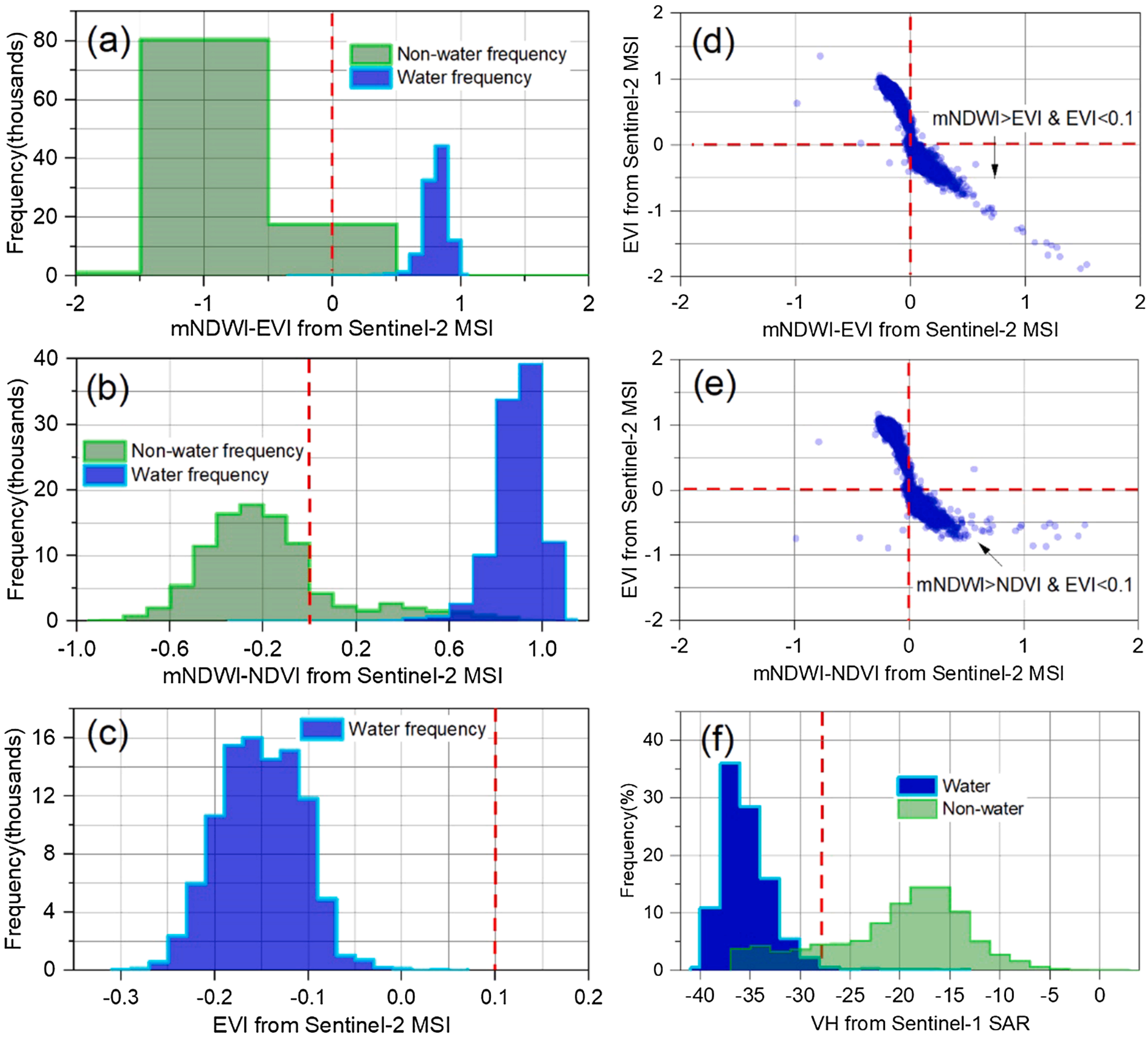

Fig. 5. (a) Frequency distribution of (mNDWI-EVI) for water and non-water sampling pixels. (b) Scatter density plots of EVI and (mNDWI-EVI) of all sampling pixels. (c) Frequency distribution of (mNDWI-NDVI) for water and non-water sampling pixels. (d) Scatter density plots of EVI and (mNDWI-NDVI) of all sampling pixels. (e) Frequency distribution of EVI for water sampling pixels. (f) Frequency distribution of the VH band from S1for water and non-water sampling pixels.

Table 2
An overview of the RTSC algorithms used to generate surface water and vegetation.

Land cover	Mapping algorithms	References
Vegetation	LSWI > 0 and EVI ≥ 0.1 and NDVI ≥ 0.2	Xiao et al., 2009; Wang et al. (2020a, b,c); Zhang et al., 2020; Liu et al., 2020
Surface water	(mNDWI > EVI) or (mNDWI > NDVI) and (EVI < 0.1)	Zou et al., 2018; Wang et al. (2020a, b,c)

3.2. Annual frequency estimates of surface water bodies and coastal vegetation

Tidal dynamics, vegetation phenology, and infrequent observations present great challenges to the capturing of coastal land cover features using a single image (Wang et al., 2020a; Liu et al., 2020). For this reason, time series image data are widely used to track land surface dynamics (Zhu and Woodcock, 2014; Kuenzer et al., 2015). The QA60 bit-mask band was used to identify those observations covered by opaque and cirrus clouds, which are considered bad-quality observations (Traganos et al., 2018). The remaining observations are considered to be good-quality observations (Jia et al., 2021). Here, the combination of S1/2 time series data produced an accurate open surface water body for each year using Eq. (5), from which the water body frequency was calculated using Eq. (6).

$$\sum \text{Water} = \begin{cases} 1\ (\text{MSI}_{\text{EVI}<0.1}) \text{ and } \left[(\text{MSI}_{\text{mNDWI}} > \text{MSI}_{\text{EVI}}) \text{ or } (\text{MSI}_{\text{mNDWI}} > \text{MSI}_{\text{NDVI}})\right] \text{ and } (\text{SAR}_{\text{VH}<-28}) \\ 0 \text{ Other values} \end{cases} \quad (5)$$

$$\text{F}_{\text{water}} = \frac{\sum \text{water}}{\sum \text{good}} \quad (6)$$

Here, $\sum$water is the observations of water calculated using Eq. (5), F_{water} is the frequency of the water (Eq. (6)),$\sum_{\text{good}}$ is the number of annual valid observations. Thus, we identified those pixels with masked out invalid observations, or excluded them from this study. In the same way, the coastal vegetation frequency was calculated using Eq. (7) and Eq. (8).

$$\sum \text{vegetation} = \begin{cases} 1\ \text{MSI}_{\text{EVI}} \geqslant 0.1 \text{ and } \text{MSI}_{\text{NDVI}} \geqslant 0.2 \text{ and } \text{MSI}_{\text{LSWI}} > 0 \\ 0 \text{ Other values} \end{cases} \quad (7)$$

$$F_{vegetation} = \frac{\sum vegetation}{\sum good} \tag{8}$$

3.3. Classification of coastal land cover

We used a straightforward coastal land cover classification scheme (tidal flats, coastal vegetation, and surface water) with different water and vegetation frequencies. The frequency maps of the open surface water calculated using the MSI and SAR images for the reference year of 2019 and the 5-year (2015–2019) average showed similar spatial patterns (Fig. 6). It is worth noting that the boundary between coastal water and non-water in the SAR images frequency map was more accurate than that of the MSI frequency map. Therefore, we combined the optical and microwave images to determine the year-long seawater and intertidal zone using the water frequency in each year.

First, we evaluated different frequency thresholds for the S1/2 images to identify surface water using the year 2019 as a reference. Previous studies in China used the value of 75 % to identify inland freshwater (Wang et al., 2020b), and 95 % was used to identify year-long seawater (Wang et al., 2020a). However, we found that S2 pixels with surface water frequency with values ≥90 % presented a relatively stable inter-annual variation (Fig. 7 a and c). Frequency maps with VH < −28 were generated based on the S1 data, and almost the water frequency with values ≥ 50 % had a very minor change (Fig. 7 b and d). Thus, we used $Fwater_{MSI} \geqslant 90\%$ and $Fwater_{SAR} \geqslant 50\%$ to define the year-long seawater. We also used 5 % of water frequency to generate the mean high-water spring tide line because the potential error range caused by the methods was assumed (Fig. 1) (Wang et al., 2020a). Therefore, water pixels with a frequency of $[(5\% \leqslant Fwater_{MSI} < 90\%)$ and $(Fwater_{SAR} < 50\%)]$ were classified as part of the coastal intertidal zone.

Second, year-long water was obtained using a threshold of 90 % from the S2 frequency map and a threshold of 50 % for the S1 frequency map to differentiate inland water such as aquaculture ponds and rivers. Therefore, water pixels with the frequency $(Fwater_{MSI} \geqslant 90\%) \cap (Fwater_{SAR} \geqslant 50\%)$ were classified as year-long water.

Third, relatively large coastal vegetation and tidal flats were selected to analysis their characteristics of water frequency and vegetation frequency (Fig. 8 a-c). According to the feature of water frequency and vegetation frequency of the sample points, the value of 15 % was used to classify tidal flats and coastal vegetation (e.g., water frequency from MSI ≤ 20 %, Fig. 8d; water frequency from SAR ≤ 10 %, Fig. 8e, and vegetation frequency < 15 %, Fig. 8f). Therefore, coastal land cover mapping algorithms of coastal vegetation, tidal flats, and year-long water were calculated using Eqs. (9), (10) and (11), respectively.

$$\text{Year-long water} = Fwater_{MSI} \geqslant 90\% \cap Fwater_{SAR} \geqslant 50\% \tag{9}$$

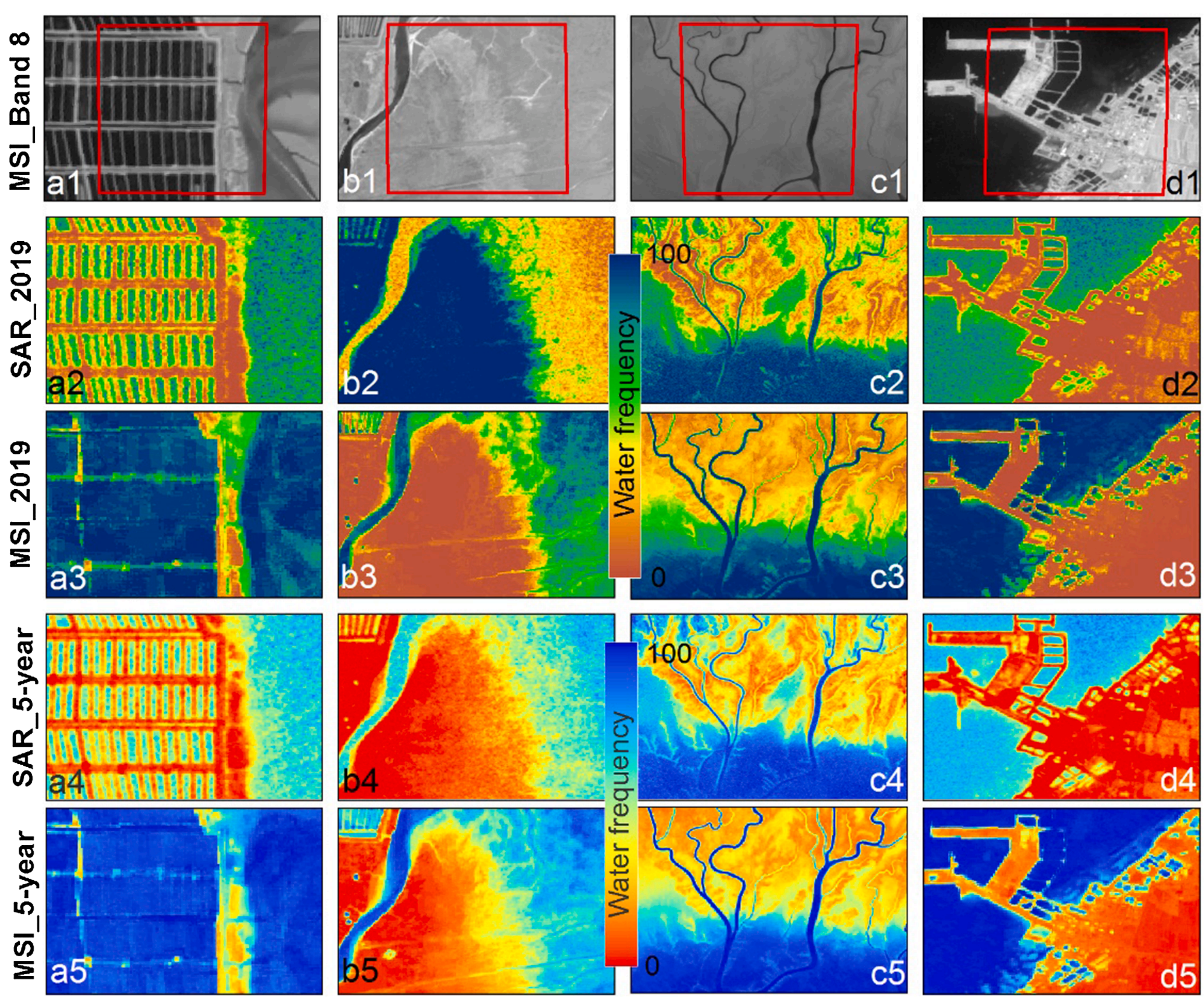

Fig. 6. Frequency maps of the open surface water. (a1–d1) S2 (MSI) band 8 of four different regions; (a2–d2) S1 (SAR) water frequency map in 2019, (a3–d3) MSI water frequency map in 2019, (a4–d4) 5-year frequency map of SAR surface water during 2015–2019, (a5–d5) 5-year frequency map of MSI surface water during 2015–2019.

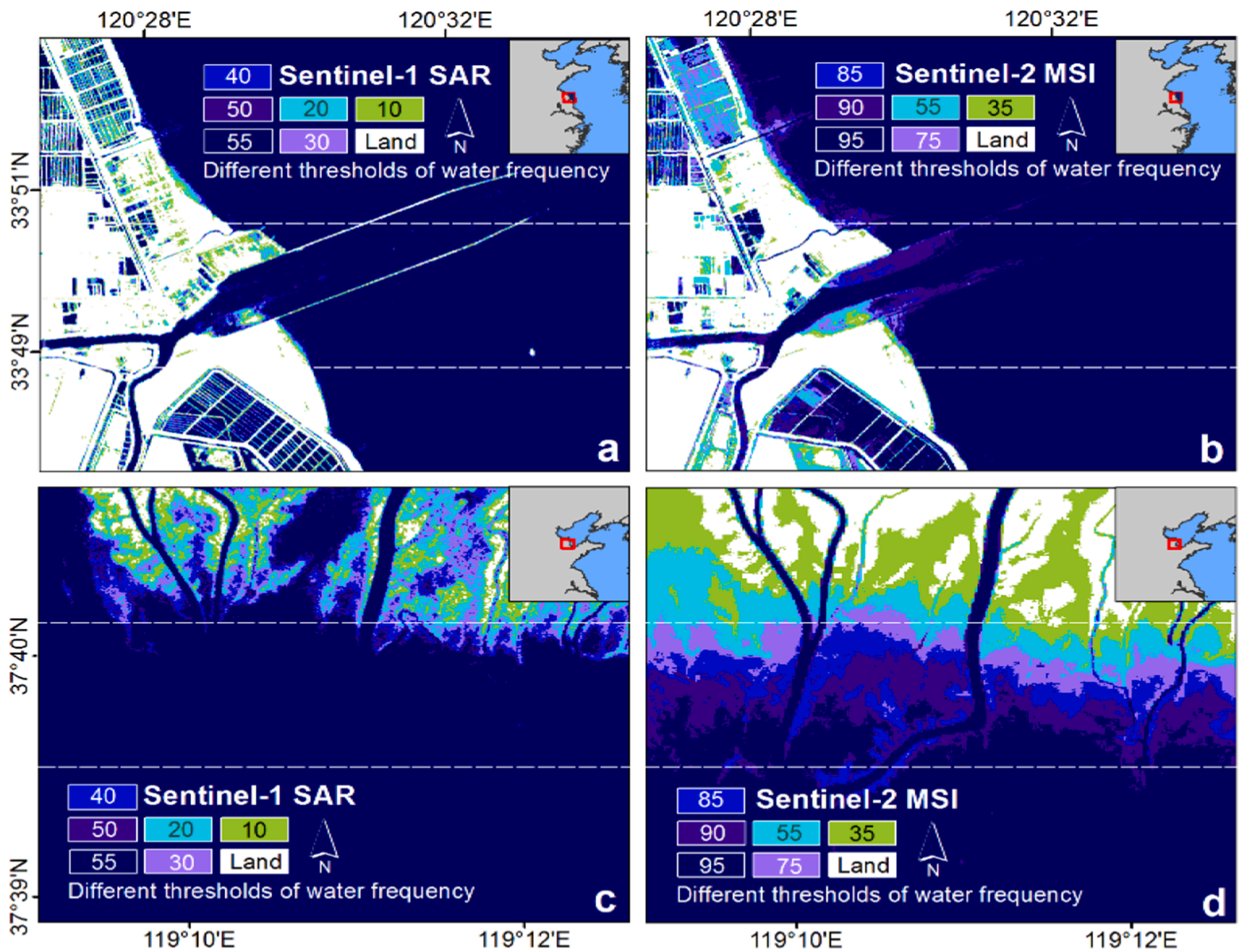

Fig. 7. Example of surface water body areas obtained using different frequency thresholds.

$$\text{Vegetation} = 15\% \leqslant \text{Fvegetation}_{\text{MSI}} \cap \text{Fwater}_{\text{MSI}} \leqslant 20\% \cap \text{Fwater}_{\text{SAR}} \leqslant 10\% \tag{10}$$

$$\text{Tidal flats} = \text{Fvegetation}_{\text{MSI}} < 15\% \cap (5\% \leqslant \text{Fwater}_{\text{MSI}} < 90\% \cap \text{Fwater}_{\text{SAR}} < 50\%) \tag{11}$$

3.4. Implementation of coastal land cover maps of the Yellow Sea for 2015–2019

Generally, the boundary between sea and land on the bedrock coast was clearly distinguishable in the remote sensing images. However, sandy, estuary, and muddy coasts have flat terrain, with more silt and sand and wetland vegetation, which is difficult to identify in the image. Artificial structures (e.g., reclamation and aquaculture ponds) on the seaside can be visually interpreted to form artificial shorelines that distinguish the boundaries of reclamation areas and intertidal zones. Meanwhile, we used buffer of artificial shorelines for the seaside boundary (Chen et al., 2019; Wang et al., 2020c). Existing research shows that if the effective observation of coastal pixels can detect the frequent occurrence of coastal surface water during the entire period (Pekel et al., 2016), then “water occurrence” can be used as an inland boundary (Mentaschi et al., 2018) (Fig. S4). Therefore, regarding the landside boundary of the coastal zone in this study, the maximum impact ranges for tides and storm surges are considered to be more effective and suitable criteria. Finally, we processed all the images using the algorithms described in Eqs.(9), (10) and (11) to generate annual coastal land cover maps of the YS between 2015 and 2019.

3.5. Validation of coastal land cover maps in 2019 and inter-comparison with other maps

We used the stratified random sampling points approach (Murray et al., 2019; Wang et al., 2020a,b,c; Liu et al., 2020) and Google Earth images each year to assess the accuracy of the YS coastal land cover map. The procedure used was as follows. (*i*) The results of this study are partitioned into three types only (tidal flats, vegetation, and year-long water). (*ii*) Random points were formed in each class using ArcGIS, and then we translated them into 10-m circle buffers of the sample points as the pixel samples. A total of 5822 validation areas of samples each year were generated for the validation of three coastal land cover map layers (Fig. S5). (*iii*) Each pixel sample for each year was checked against historical Google Earth imagery for the corresponding year and labeled as the pure coastal land cover pixel sample to avoid the sampling error caused by yearly surface changes. (*iv*) A confusion matrix was calculated to validate the accuracy of the results (see Section 4.1 for further information).

After obtaining the data of coastal land cover based on microwave and optical time series images, they were compared with other relevant land cover datasets in the scope of the study area. Table 3 lists general information about the land cover datasets included for comparison. The 2017 10 m FROM-GLC10 map (Gong et al., 2019) was developed at Tsinghua University (THU), using S2 images in GEE. In the FROM-

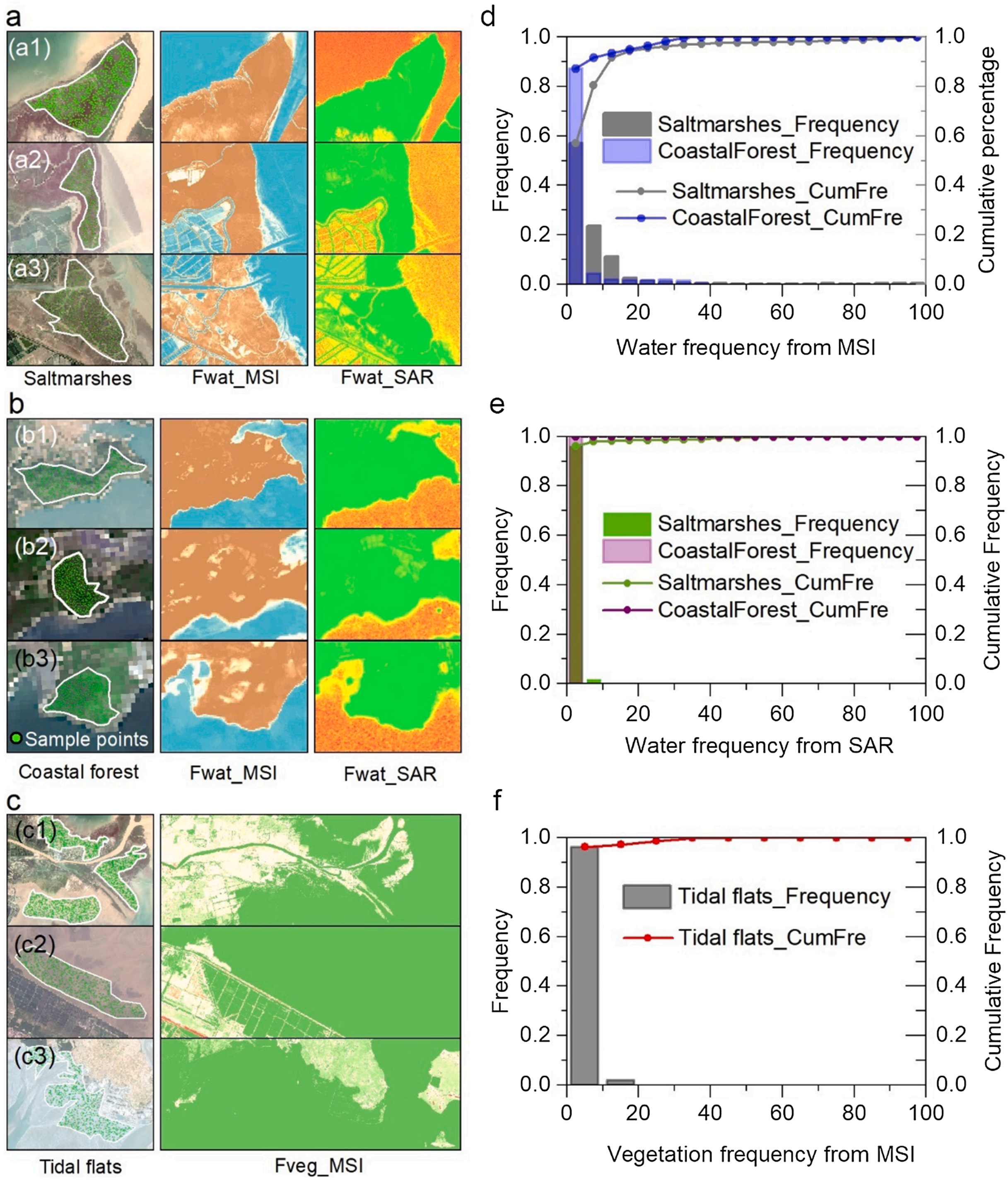

Fig. 8. Location of selected coastal vegetation and tidal flats validation areas of samples and their pixels with varying annual good-quality observations of water and vegetation frequency distribution. (a) saltmarsh vegetation; (b) coastal forest vegetation; (c) tidal flats; (d) MSI water frequency map of saltmarsh and coastal forest; (e) SAR water frequency map of saltmarsh and coastal forest; (f) MSI vegetation frequency map of tidal flats.

GLC10 map, coastal vegetation classes such as cropland, forest, grassland, and shrubland were included. Therefore, we compared the coastal vegetation areas defined in FROM-GLC10 with the vegetation areas that we obtained in our dates (NBU/OU map) in 2017 and in the same regions. The global tidal flats dataset from 1984 to 2016 was developed by the University of Queensland (UQ) (Murray et al., 2019), using Landsat images in GEE and random forest algorithms. Therefore, we analyzed the tidal flats map the NBU/OU dataset (2015–2016) and the UQ tidal flats dataset (2014–2016). The China 1 km land cover map in 2015 (CAS map) was developed by the Chinese Academy of Sciences (CAS) using Landsat-8 OLI images. In this case, we compared the areas of tidal flats from the CAS map with the areas of the tidal flats we identified in our coastal land cover map (NBU/OU map) in the same year (2015–2016). China's coastal wetland maps (1986–2016) were developed by Fudan University (FU) and the University of Oklahoma (OU). This dataset used Landsat ETM+/OLI images in the GEE. We compared the areas of tidal flats in northern China from coastal wetland maps (FU/OU-CoastalWetland map) and our coastal land cover map (NBU/OU coastal land cover map) in 2018. The tidal flats in northern China for 2015 (Zhang et al., 2019) were developed by Shenzhen University (SZU) and included

Table 3
Datasets of the land cover maps included for comparison.

Map name	References/ Study area	Data/Time	Comparison with this study
FROM-GLC10 map	Gong et al. (2019)/ Global**	Sentinel–2/ 2017	Vegetation in the coastal zone+; 2017# versus 2017*
UQ tidal flats map	Murray et al. (2019)/ Global**	Landsat/ 1986–2016	Tidal flats+; 2015–2016# versus 2014–2016*
CAS map	Chinese Academy of Sciences/ China▲	Landsat/2015	Tidal flats+; 2015–2016# versus 2015*
FU/OU-TidalFlats map	Wang et al., (2020a)/ China▲	Landsat/ 1986–2016	Tidal flats+; 2015–2016# versus 2016*
FU/OU-CoastalWetland map	Wang et al., (2020b)/ China▲	Landsat/2018	Tidal flats+; 2018# versus 2018*
SZU map	Zhang et al., (2019)/China	Landsat/2015	Tidal flats+; 2015–2016# versus 2015*
NBU/OU map	This study/ Yellow Sea	Sentinel–1&2/ 2015–2019	Vegetation in the coastal zone+; 2017# versus 2017*; Tidal flats+; 2015–2016# versus 2015*

+Objects and different area in China around the YS coastal zone were compared; #This study was used; *Related studies were used; **The random forest method was used; ▲Visual interpretation method was used; NBU: Ningbo University.

mapped tidal flats in northern China (SZU map) using Landsat 8 OLI images and GEE.

4. Results

4.1. Map of coastal land cover types and accuracy assessment

The accuracy of the coastal land cover map during 2015–2019 was evaluated using the validation areas of samples described in Section 3.5. The confusion matrix revealed that the 2019 map had high overall accuracy. The producer's accuracy and user's accuracy for the coastal year-long water were 97 % and 99 %, respectively, and they were higher than those for the coastal vegetation. Tidal flats had a slightly lower accuracy among the three coastal land cover types (i.e., user's accuracy of 92 % and producer's accuracy of 94 %), because several water points with very low water frequency were classified as coastal year-long water. As far as the specific accuracy evaluation results of each year are concerned, it is shown in Table 4.

Fig. 9 shows the coastal land cover details in seven typical regions and Fig. 10 lists the areas of the various types in each section in 2019. The total area of coastal land cover types in YS in 2019 was determined, which included 3593.42 km^2 of tidal flats, 28,506.98 km^2 of coastal vegetation, and 5436.92 km^2 of year-long water. Section B had the largest coastal land cover area in the YS, this area is the region with the most special development of sedimentary landform system and the most abundant tidal flats resources in China, with many tidal flat and salt marsh vegetation distributed, followed by section I, D, A, C, H, G, F and E. The vegetation in the YS was distributed mainly along the coastlines of Sections B, D, and I. Section B had the largest coastal year-long water area, followed by Sections C, D, G, A, I, H, E and F. Tidal flats were mainly distributed in Sections I, H, B, A, C, F, G, E and D. Section F had the smallest coastal land cover area in the YS, as well as the smallest area of year-long water.

4.2. Interannual changes in coastal land cover areas during 2015–2019

From the perspective of the spatial distribution pattern of land cover

Table 4
Confusion matrix for assessing coastal land cover mapping algorithms.

Year	Classification	Reference			Use. acc.	Ove. acc.
		Tidal flats	Vegetation	Year-long water		
2015	Tidal flats	1514	135	124	85	92
	Vegetation	92	1388	50	91	
	Year-long water	56	5	2458	98	
	Pro. acc.	91	91	99		
2016	Tidal flats	1514	145	114	85	92
	Vegetation	92	1392	46	91	
	Year-long water	41	3	2475	98	
	Pro. acc.	92	90	94		
2017	Tidal flats	1635	88	50	92	95
	Vegetation	79	1432	19	94	
	Year-long water	40	0	2479	98	
	Pro. acc.	93	94	97		
2018	Tidal flats	1596	126	51	90	94
	Vegetation	66	1443	21	94	
	Year-long water	69	2	2448	97	
	Pro. acc.	93	92	97		
2019	Tidal flats	1632	86	55	92	95
	Vegetation	66	1440	24	94	
	Year-long water	37	0	2482	99	
	Pro. acc.	94	94	97		

Use. acc. -User's accuracy (%); Ove. acc.-overall accuracy (%); Pro. acc.- Producer's accuracy (%).

information along the YS coastal zone (Fig. 11), the areas with large interannual variations in the total land cover of the YS coast are mainly distributed in northeastern China, North Korea, and western South Korea between 2015 and 2019. On the one hand, limited by the time of the data source, there are limitations in revealing the changing trend of the land cover in the coastal zone on a five-year scale. more significantly, resulting in changes in coastal land cover. The total annual coastal land cover area varied from 2.42 $\times$ 10^4 km^2 in 2016 (the missing data for 2015 represented only 1.65 $\times$ 10^4 km^2) to 3.75 $\times$ 10^4 km^2 in 2019, with an average area of 2.49 $\times$ 10^4 km^2.

The interval of 2015–2019 shows the following: (1) a stable section (section D), the area is dominated by vegetation and perennial seawater, with a small area of tidal flats, and the landcover area of the coastal zone changed little during the study period; (2) increases in section A and section B, the vegetation in the two areas is mainly farmland and salt marshes in the reclamation area, and most of the increase comes from the increase in the area of tidal flats; and (3) decreases in section C, section E, section F, section G, section H and section I. During the development of these regions, different land cover types showed different trends over five years. Among them, in section C, section E, section F, and section G areas, the land cover area of the coastal zone is reduced due to the reduction of aquaculture ponds and salt marsh vegetation. In parts section H and section I, reclamation provides bearing space for alleviating the pressure on coastal land, increasing the supply of food or aquatic products, but causing the reduction of coastal vegetation and year-long water. Although the protection and ecological restoration of coastal wetlands along the coast of the YS has been continuously strengthened in recent years, the trend of loss of coastal vegetation, tidal flats, and year-long water areas is still severe.

4.3. Comparison with other maps

Wang et al. (2020a,b) generated annual maps of tidal flats (FU/OU-Tidal Flats) and a map of coastal wetlands in China using Landsat images (FU/OU-Coastal Wetland) (Fig. 12). We obtained the areas of the tidal flats in China for 2015 and 2018 from these studies and compared them

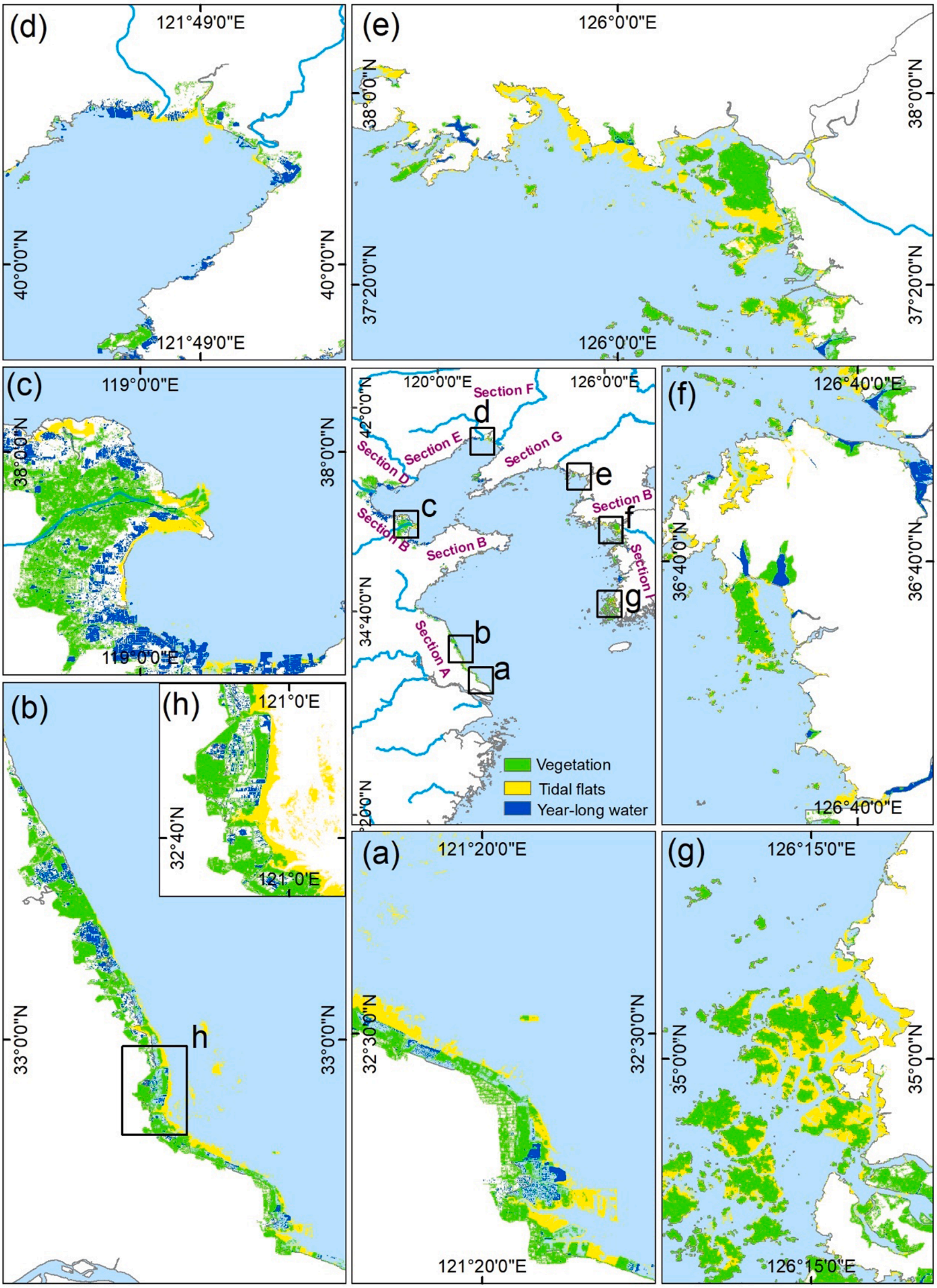

Fig. 9. Typical coastal land cover, displaying the distribution patterns of vegetation, tidal flats, and year-long water.

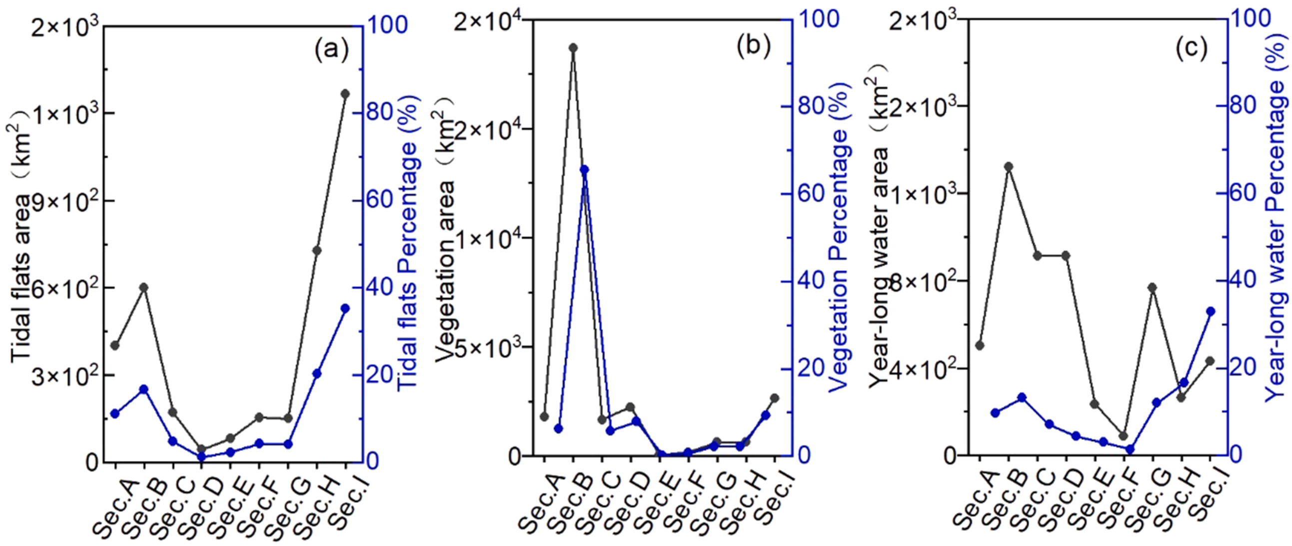

Fig. 10. Distribution of coastal land cover types in different regions of the YS in 2019. Sec. A-I means section A-I.

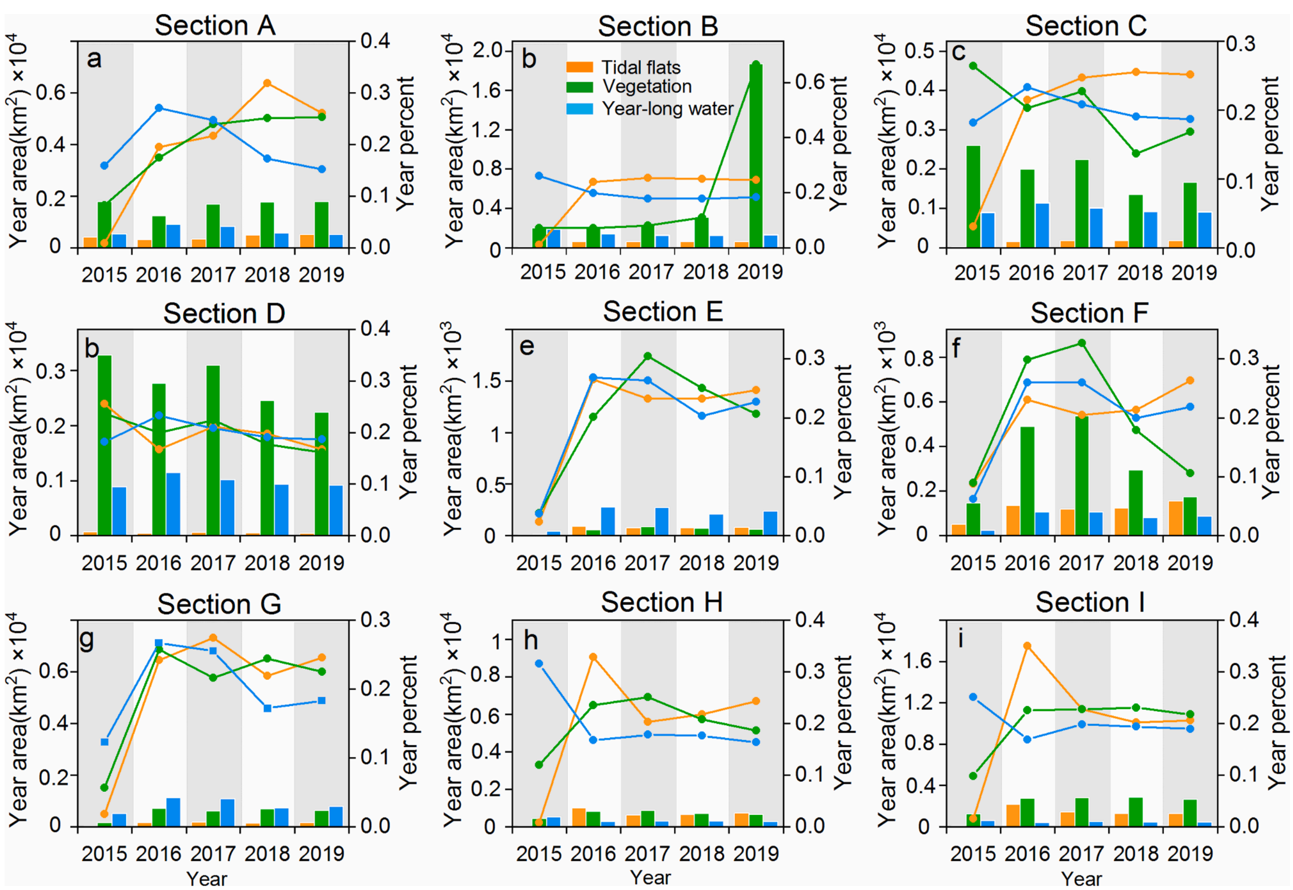

Fig. 11. Inter-annual variations of the area of coastal land cover in the different sections. Year percent is the ratio of single type areas to total areas in the YS during 2015–2019.

to NBU/OU maps. The FU/OU-Tidal Flats map reported tidal flats area of 887.5 km^2, while our dataset estimated the area of tidal flat area of 835.0 km^2 in 2015. However, we detected a smaller tidal flat area in our dataset (723.6 km^2) than in the FU/OU-CoastalWetland map (823.2 km^2) in 2018(Fig. 12a).; this is because the 10 m spatial resolution S2 image can detect more open surface water bodies than the 30 m Landsat image. Moreover, S1 can overcome the influence of clouds and rain, and capture open surface water bodies with a greater frequency. Thus, the tidal flat area in this study is relatively low.

From our maps, the total area of tidal flats was 1140 km^2 less than in the FU/OU-CoastalWetland map (Wang et al., 2020b) in 2017, but the vegetation area was 3455 km^2 larger than in the FROM-GLC10 map (Gong et al., 2019) in 2018. This difference can be attributed mainly to the number of RS images and algorithms used for coastal wetland

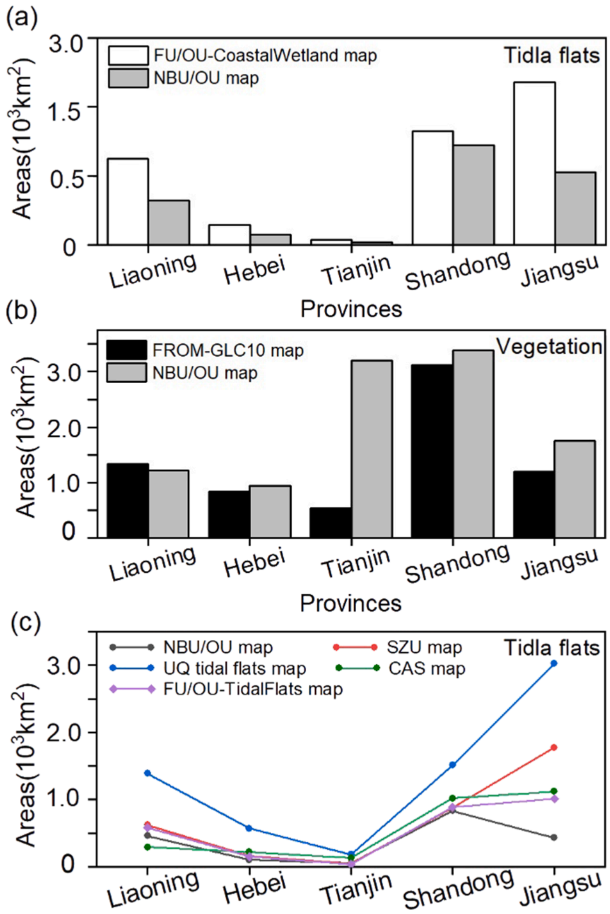

Fig. 12. Comparison of the land cover area of the coastal zone between the dataset obtained in this study and other maps in the provinces of China on the YS. (a) Comparison of the tidal flats between our study and the FU/OU-CoastalWetland map in 2018. (b) Comparison of the vegetation cover between our study and that of FROM-GLC10 map in 2017. (c) Comparison of the areas of tidal flats between our map in 2015 and the UQ tidal flats map for 2014–2016, FU/OU-TidalFlats map, the SZU map in 2015, and the CAS map in 2015.

mapping (Fig. 12b). Compared with the report on the FU/OU-CoastalWetland map using only Landsat images, the combination of a large number of optical and microwave Sentinel images in this study provides more good-quality observations during the same time interval. As a result, the area of tidal flats decreased in view of the inundation of water bodies, and the area of vegetation increased due to the increased probability of being detected.

The results obtained in this study are very similar to those obtained by Zhang et al. (2019), who mapped coastal wetlands in the SZU map in 2015 using the random forest algorithm(Fig. 12c). The tidal flat areas in the NBU/OU map were well matched with the area of the CAS map and FU/OU-TidalFlats map for the provinces of northern China in 2015. The tidal flats area in the UQ tidal flats map was 6678.1 km^2, while in our study it was 1882.7 km^2. It is worth noting that only Jiangsu Province had a smaller area of tidal flats in our map than in the other datasets.

5. Discussion

5.1. Materials and methods for mapping coastal land cover

Comparison of our maps with others demonstrated some differences (Fig. 13). We used an RTSC method to classify coastal land cover and combined S1/2 time-series images to detect tidal flats, whereas the UQ tidal flats map used the random forest method to identify tidal flats. These differences contributed to the discrepancies between the NBU/OU map and the UQ tidal flats map (Fig. 13a1–c2). The coastal vegetation area of our dataset was highly consistent with the FROM-GLC10 map (Fig. 12b and Fig. 13a1 and a3). On the other hand, the SZU map used a seaward (40 km) and landward (10 km) buffer along the coastline, while we used a “water occurrence” as the inland boundary (Pekel et al., 2016; Mentaschi et al., 2018) and the buffer of artificial shorelines as a seaside boundary, resulting in a large difference in the area of tidal flats. Therefore, the comparison of these maps showed that it is necessary to generate detailed maps of coastal land cover types to better reduce the data and algorithms on changes in coastal land cover types.

5.2. Uncertainties in coastal land cover mapping

The uncertainty of coastal land cover maps of the YS is influenced by several factors, including type and quantity of RS data, algorithm, and the classification schemes of coastal land cover. In this study, although using the QA60 bitmask band removed most of the bad observations (Traganos et al., 2018), it was impossible to remove all of them because of the limited character of the band. S1 data are very sensitive to water and non-water cover (e.g., cropland, saltmarsh, and lowland forest) (Reiche et al., 2018; Veloso et al., 2017; Chen et al., 2017), and according to the water and non-water areas of samples in 2019, surface water can be readily identified based on VH < -28 (Fig. 5f). Nevertheless, a few lands cover types, such as muddy and beaches, also have VH < -28 (Fig. S3).

The tidal variations within scenes could also introduce doubtfulness into coastal wetlands mapping (Wang et al., 2018; Liu et al., 2015; Jia et al., 2021). However, our RTSC mapping method utilized all the available S1/2 data to reduce those impacts. Besides, the threshold of $\mathrm{Fwater_{MSI}} = 90$ and $\mathrm{Fwater_{SAR}} = 50$ was used to identify tidal flats and year-long seawater. This value can result in a mixture of tidal flats and open surface water when there are areas of coastal water with very low Fwater in some years (Wang et al., 2020c).

5.3. Future applications in coastal land cover mapping

The RTSC algorithm and S1/2 time-series images have a potentially wide range of applications as the data available increases. These applications include mapping coastal land cover and monitoring changes coastline in multiple regions and other years. Regarding the coastal land cover mapping in other regions, the Classification tool can be employed by tuning the thresholds of the RTSC-related metrics using regional areas of samples. This is supported by recent studies using phenology-based approaches to map various major coastal land cover types at coarser resolution (Chen et al., 2017; Wang et al., 2020b; Zhang et al., 2020). Currently, miscellaneous deep learning models and machine learning are being deliberated for coastal cover mapping (Feng et al., 2019; Pashaei et al., 2020). This coastal land cover mapping flow can be replaced by coordinating the RTSC parameters and machine learning models to classify coastal land cover in future longer time series research.

6. Conclusions

Obtaining accurate and timely information about the composition and distribution of coastal land cover is essential for effective coastal sustainability and ecological protection. Moreover, there is a need to track the changes of coastal land cover over a large scale. We developed an RTSC coastal land cover mapping algorithm, which uses time-series microwave images S1 and optical images S2 to identify and map coastal land cover types. We generated a more detailed annual map of coastal land cover during 2015–2019 with a 10 m resolution in the Yellow Sea. This study demonstrates that the combination of S1/2 can provide an adequate number of valid observations for coastal land-cover mapping. Moreover, the relatively high spatial resolution and revisit

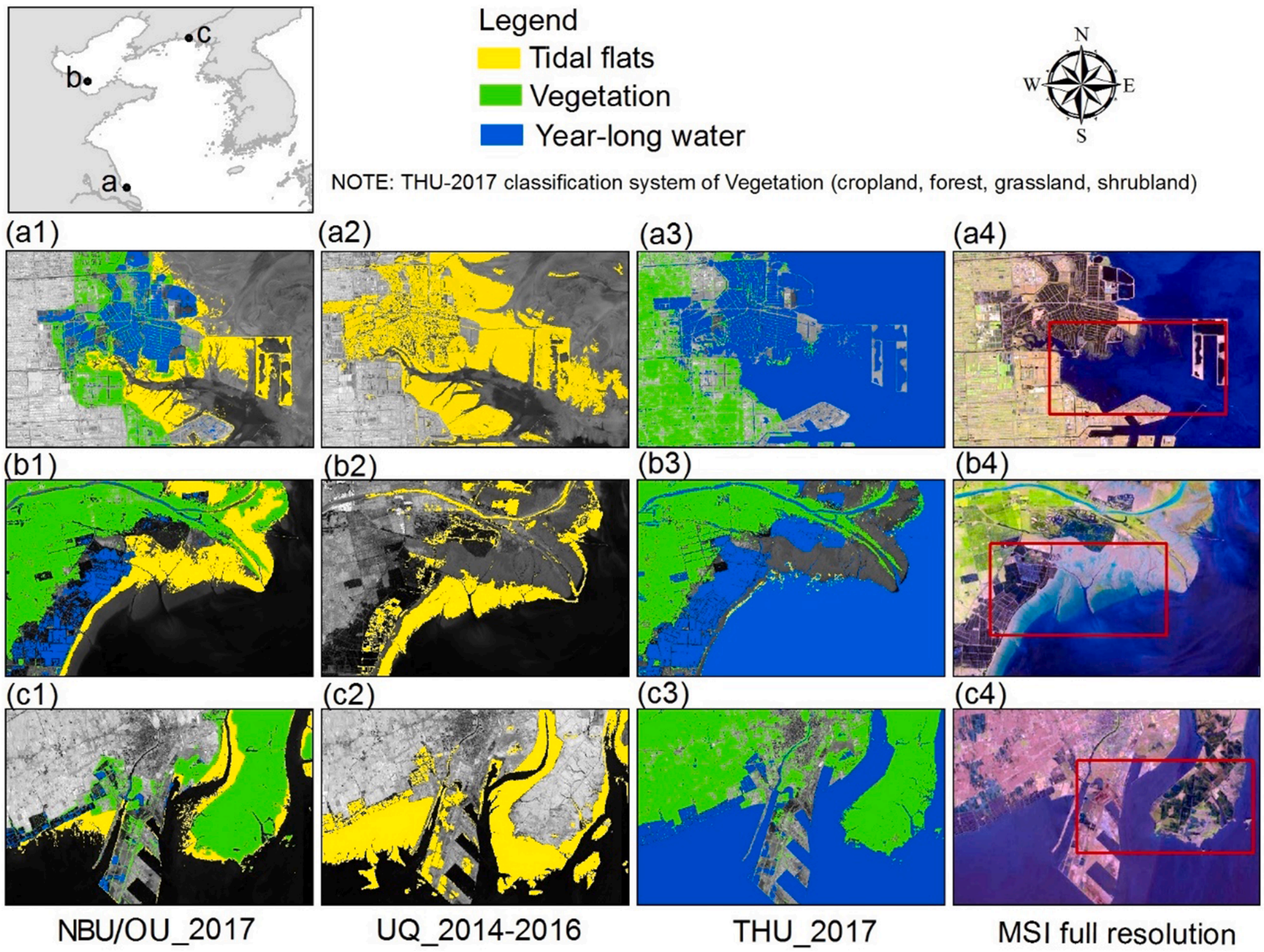

Fig. 13. Zoom-in views of coastal land cover from the NBU/OU map in 2017, the UQ tidal flats map from the UQ during 2014–2016, and the global land cover from THU in 2017.

time are useful for detecting small-scale features and areas affected by frequent cloud cover, wind, waves, and tides. The developed RTSC coastal land cover mapping method has the potential to be applied to the mapping of coastal land cover in other years and at other locations, globally. The resulting maps provide fundamental information for coastal conservation and management, and for policymakers and stakeholders..

Declaration of Competing Interest

The authors declare that they have no known competing financial interests or personal relationships that could have appeared to influence the work reported in this paper.

Acknowledgments

This research was supported by the National Natural Science Foundation of China (42206236, 41971378, 41976209), the Fundamental Research Funds for the Provincial Universities of Zhejiang (SJWY2022012), the China Postdoctoral Science Foundation (2021M700835, 2021TQ0072), the Ningbo Natural Science Foundation, China (2022J092, 2022J075), the Science and Technology Major Project of Ningbo,China (2021Z181), and the US National Science Foundation (1911955).

Appendix A. Supplementary material

Supplementary data to this article can be found online at https://doi.org/10.1016/j.isprsjprs.2022.12.029.

References

Adger, W.N., Hughes, T.P., Folke, C., Carpenter, S.R., Rockström, J., 2005. Social-ecological resilience to coastal disasters. Science (80-). https://doi.org/10.1126/science.1112122.

Amani, M., Salehi, B., Mahdavi, S., Brisco, B., 2018. Spectral analysis of wetlands using multi-source optical satellite imagery. ISPRS J. Photogramm. Remote Sens. 144, 119–136.

Arino, O., Bicheron, P., Achard, F., Latham, J., Witt, R., Weber, J.L., 2008. GlobCover: The Most Detailed Portrait of Earth. Eur. Sp. Agency Bull.

Bhargava, R., Sarkar, D., Friess, D.A., 2020. A cloud computing-based approach to mapping mangrove erosion and progradation: Case studies from the Sundarbans and French Guiana. Estuar. Coast. Shelf Sci. 106798.

Bansal, S., Katyal, D., Garg, J.K., 2017. A novel strategy for wetland area extraction using multispectral MODIS data. Remote Sens. Environ. https://doi.org/10.1016/j.rse.2017.07.034.

Bartholomé, E., Belward, A.S., 2005. GLC2000: a new approach to global land cover mapping from earth observation data. Int. J. Remote Sens. https://doi.org/10.1080/01431160412331291297.

Bauer, J.E., Cai, W.J., Raymond, P.A., Bianchi, T.S., Hopkinson, C.S., Regnier, P.A.G., 2013. The changing carbon cycle of the coastal ocean. Nature. https://doi.org/10.1038/nature12857.

Bergsma, Erwin, W.J., Almar, R., 2020. Coastal coverage of ESA' Sentinel 2 mission. Adv. Sp. Res. https://doi.org/10.1016/j.asr.2020.03.001.

Bontemps, J.D., Hervé, J.C., Dhôte, J.F., 2010. Dominant radial and height growth reveal comparable historical variations for common beech in north-eastern France. For. Ecol. Manage. https://doi.org/10.1016/j.foreco.2010.01.019.

Brombacher, J., Reiche, J., Dijksma, R., Teuling, A.J., 2020. Near-daily discharge estimation in high latitudes from Sentinel-1 and 2: a case study for the Icelandic Þjórsá River. Remote Sens. Environ. https://doi.org/10.1016/j.rse.2020.111684.
Chen, Y., Dong, J., Xiao, X., Ma, Z., Tan, K., Melville, D., Li, B., Lu, H., Liu, J., Liu, F., 2019. Effects of reclamation and natural changes on coastal wetlands bordering China's Yellow Sea from 1984 to 2015. L. Degrad. Dev. https://doi.org/10.1002/ldr.3322.
Chen, B., Xiao, X., Li, X., Pan, L., Doughty, R., Ma, J., Dong, J., Qin, Y., Zhao, B., Wu, Z., Sun, R., Lan, G., Xie, G., Clinton, N., Giri, C., 2017. A mangrove forest map of China in 2015: Analysis of time series Landsat 7/8 and Sentinel-1A imagery in Google Earth Engine cloud computing platform. ISPRS J. Photogramm. Remote Sens. https://doi.org/10.1016/j.isprsjprs.2017.07.011.
Chen, M., Ke, Y., Bai, J., Li, P., Lyu, M., Gong, Z., Zhou, D., 2020. Monitoring early stage invasion of exotic Spartina alterniflora using deep-learning super-resolution techniques based on multisource high-resolution satellite imagery: A case study in the Yellow River Delta, China. Int. J. Appl. Earth Obs. Geoinf. https://doi.org/10.1016/j.jag.2020.102180.
Choi, J.K., Park, Y.J., Lee, B.R., Eom, J., Moon, J.E., Ryu, J.H., 2014. Application of the Geostationary Ocean Color Imager (GOCI) to mapping the temporal dynamics of coastal water turbidity. Remote Sens. Environ. https://doi.org/10.1016/j.rse.2013.05.032.
Feng, Q., Yang, J., Zhu, D., Liu, J., Guo, H., Bayartungalag, B., Li, B., 2019. Integrating multitemporal Sentinel-1/2 data for coastal land cover classification using a multibranch convolutional neural network: a case of the Yellow River Delta. Remote Sens. https://doi.org/10.3390/rs11091006.
Friedl, M.A., Sulla-Menashe, D., Tan, B., Schneider, A., Ramankutty, N., Sibley, A., Huang, X., 2010. MODIS Collection 5 global land cover: algorithm refinements and characterization of new datasets. Remote Sens. Environ. https://doi.org/10.1016/j.rse.2009.08.016.
Gong, P., Wang, J., Yu, L., Zhao, Y., Zhao, Y., Liang, L., Niu, Z., Huang, X., Fu, H., Liu, S., Li, C., Li, X., Fu, W., Liu, C., Xu, Y., Wang, X., Cheng, Q., Hu, L., Yao, W., Zhang, H., Zhu, P., Zhao, Z., Zhang, H., Zheng, Y., Ji, L., Zhang, Y., Chen, H., Yan, A., Guo, J., Yu, L., Wang, L., Liu, X., Shi, T., Zhu, M., Chen, Y., Yang, G., Tang, P., Xu, B., Giri, C., Clinton, N., Zhu, Z., Chen, J., 2013. Finer resolution observation and monitoring of global land cover: first mapping results with Landsat TM and ETM+ data. Int. J. Remote Sens. https://doi.org/10.1080/01431161.2012.748992.
Gong, P., Liu, H., Zhang, M., Li, C., Wang, J., Huang, H., Clinton, N., Ji, L., Li, W., Bai, Y., Chen, B., Xu, B., Zhu, Z., Yuan, C., Ping Suen, H., Guo, J., Xu, N., Li, W., Zhao, Y., Yang, J., Yu, C., Wang, X., Fu, H., Yu, L., Dronova, I., Hui, F., Cheng, X., Shi, X., Xiao, F., Liu, Q., Song, L., 2019. Stable classification with limited sample: transferring a 30-m resolution sample set collected in 2015 to mapping 10-m resolution global land cover in 2017. Sci. Bull. https://doi.org/10.1016/j.scib.2019.03.002.
Han, Q., Niu, Z., Wu, M., Wang, J., 2019. Remote-sensing monitoring and analysis of China intertidal zone changes based on tidal correction. Kexue Tongbao/Chinese Sci. Bull. https://doi.org/10.1360/N972018-00723.
Held, A., Ticehurst, C., Lymburner, L., Williams, N., 2003. High resolution mapping of tropical mangrove ecosystems using hyperspectral and radar remote sensing. Int. J. Remote Sens. 24, 2739–2759.
Huete, A., Didan, K., Miura, T., Rodriguez, E.P., Gao, X., Ferreira, L.G., 2002. Overview of the radiometric and biophysical performance of the MODIS vegetation indices. Remote Sens. Environ. https://doi.org/10.1016/S0034-4257(02)00096-2.
Jevrejeva, S., Jackson, L.P., Riva, R.E.M., Grinsted, A., Moore, J.C., 2016. Coastal sea level rise with warming above 2 °C. Proc. Natl. Acad. Sci. U. S. A. https://doi.org/10.1073/pnas.1605312113.
Jia, M., Wang, Z., Mao, D., Ren, C., Wang, C., Wang, Y., 2021. Rapid, robust, and automated mapping of tidal flats in China using time series Sentinel-2 images and Google Earth Engine. Remote Sens. Environ. https://doi.org/10.1016/j.rse.2021.112285.
Kirwan, M.L., Megonigal, J.P., 2013. Tidal wetland stability in the face of human impacts and sea-level rise. Nature. https://doi.org/10.1038/nature12856.
Zou, Z., Xiao, X., Dong, J., Qin, Y., Doughty, R.B., Menarguez, M.A., Zhang, G., Wang, J., 2018. Divergent trends of open-surface water body area in the contiguous United States from 1984 to 2016. Proc. Natl. Acad. Sci. U. S. A. https://doi.org/10.1073/pnas.1719275115.
Koh, C.H., Khim, J.S., 2014. The Korean tidal flat of the Yellow Sea: Physical setting, ecosystem and management. Ocean Coast. Manag. doi: 10.1016/j.ocecoaman.2014.07.008.
Kuenzer, C., Dech, S., Wagner, W., 2015. Remote sensing time series revealing land surface dynamics: status quo and the pathway ahead. Remote Sensing Time Series 1–24.
La, T.V., Khenchaf, A., Comblet, F., Nahum, C., 2017. Exploitation of C-band sentinel-1 images for high-resolution wind field retrieval in coastal zones (Iroise Coast, France). IEEE J. Sel. Top. Appl. Earth Obs. Remote Sens. doi: 10.1109/JSTARS.2017.2746349.
Liu, Y., Zhou, M., Zhao, S., Zhan, W., Yang, K., Li, M., 2015. Automated extraction of tidal creeks from airborne laser altimetry data. J. Hydrol. https://doi.org/10.1016/j.jhydrol.2015.05.058.
Liu, Y., Liu, Y., Li, J., Lu, W., Wei, X., Sun, C., 2018. Evolution of landscape ecological risk at the optimal scale: a case study of the open coastal wetlands in Jiangsu, China. Int. J. Environ. Res. Public Health 15, 1691.
Liu, Y., Liu, Y., Li, J., Sun, C., Xu, W., Zhao, B., 2020. Trajectory of coastal wetland vegetation in Xiangshan Bay, China, from image time series. Mar. Pollut. Bull. 160, 111697.
Ma, T., Li, X., Bai, J., Cui, B., 2019. Tracking three decades of land use and land cover transformation trajectories in China's large river deltas. L. Degrad. Dev. 30, 799–810.
Mahdianpari, M., Salehi, B., Mohammadimanesh, F., Homayouni, S., Gill, E., 2019. The first wetland inventory map of newfoundland at a spatial resolution of 10 m using sentinel-1 and sentinel-2 data on the Google Earth Engine cloud computing platform. Remote Sens. https://doi.org/10.3390/rs11010043.
Mentaschi, L., Vousdoukas, M.I., Pekel, J.F., Voukouvalas, E., Feyen, L., 2018. Global long-term observations of coastal erosion and accretion. Sci. Rep. https://doi.org/10.1038/s41598-018-30904-w.
Mohammadimanesh, F., Salehi, B., Mahdianpari, M., Brisco, B., Motagh, M., 2018. Multi-temporal, multi-frequency, and multi-polarization coherence and SAR backscatter analysis of wetlands. ISPRS J. Photogramm. Remote Sens. https://doi.org/10.1016/j.isprsjprs.2018.05.009.
Murray, N.J., Clemens, R.S., Phinn, S.R., Possingham, H.P., Fuller, R.A., 2014. Tracking the rapid loss of tidal wetlands in the Yellow Sea. Front. Ecol. Environ. https://doi.org/10.1890/130260.
Murray, N.J., Phinn, S.R., DeWitt, M., Ferrari, R., Johnston, R., Lyons, M.B., Clinton, N., Thau, D., Fuller, R.A., 2019. The global distribution and trajectory of tidal flats. Nature. https://doi.org/10.1038/s41586-018-0805-8.
Nielsen, E.M., Prince, S.D., Koeln, G.T., 2019. Wetland change mapping for the U.S. mid-Atlantic region using an outlier detection technique. Remote Sens. Environ. https://doi.org/10.1016/j.rse.2008.04.017.
Niu, Z.G., Zhang, H.Y., Wang, X.W., Yao, W.B., Zhou, D.M., Zhao, K.Y., Zhao, H., Li, N.N., Huang, H.B., Li, C.C., Yang, J., Liu, C.X., Liu, S., Wang, L., Li, Z., Yang, Z.Z., Qiao, F., Zheng, Y.M., Chen, Y.L., Sheng, Y.W., Gao, X.H., Zhu, W.H., Wang, W.Q., Wang, H., Weng, Y.L., Zhuang, D.F., Liu, J.Y., Luo, Z.C., Cheng, X., Guo, Z.Q., Gong, P., 2012. Mapping wetland changes in China between 1978 and 2008. Chin. Sci. Bull. https://doi.org/10.1007/s11434-012-5093-3.
Ottinger, M., Clauss, K., Kuenzer, C., 2017. Large-scale assessment of coastal aquaculture ponds with Sentinel-1 time series data. Remote Sens. https://doi.org/10.3390/rs9050440.
Pashaei, M., Kamangir, H., Starek, M.J., Tissot, P., 2020. Review and evaluation of deep learning architectures for efficient land cover mapping with UAS hyper-spatial imagery: a case study over a wetland. Remote Sens. https://doi.org/10.3390/rs12060959.
Pekel, J.F., Cottam, A., Gorelick, N., Belward, A.S., 2016. High-resolution mapping of global surface water and its long-term changes. Nature. https://doi.org/10.1038/nature20584.
Pendleton, L., Donato, D.C., Murray, B.C., Crooks, S., Jenkins, W.A., Sifleet, S., Craft, C., Fourqurean, J.W., Kauffman, J.B., Marbà, N., Megonigal, P., Pidgeon, E., Herr, D., Gordon, D., Baldera, A., 2012. Estimating global "Blue Carbon" emissions from conversion and degradation of vegetated coastal ecosystems. PLoS ONE. https://doi.org/10.1371/journal.pone.0043542.
Prasad, K.A., Ottinger, M., Wei, C., Leinenkugel, P., 2019. Assessment of coastal aquaculture for India from Sentinel-1 SAR time series. Remote Sens. https://doi.org/10.3390/rs11030357.
Reiche, J., Hamunyela, E., Verbesselt, J., Hoekman, D., Herold, M., 2018. Improving near-real time deforestation monitoring in tropical dry forests by combining dense Sentinel-1 time series with Landsat and ALOS-2 PALSAR-2. Remote Sens. Environ. https://doi.org/10.1016/j.rse.2017.10.034.
Rokni, K., Ahmad, A., Selamat, A., Hazini, S., 2014. Water feature extraction and change detection using multitemporal landsat imagery. Remote Sens. https://doi.org/10.3390/rs6054173.
Salameh, E., Frappart, F., Turki, I., Laignel, B., 2020. Intertidal topography mapping using the waterline method from Sentinel-1 & -2 images: The examples of Arcachon and Veys Bays in France. ISPRS J. Photogramm. Remote Sens. https://doi.org/10.1016/j.isprsjprs.2020.03.003.
Schuerch, M., Spencer, T., Temmerman, S., Kirwan, M.L., Wolff, C., Lincke, D., McOwen, C.J., Pickering, M.D., Reef, R., Vafeidis, A.T., Hinkel, J., Nicholls, R.J., Brown, S., 2018. Future response of global coastal wetlands to sea-level rise. Nature. https://doi.org/10.1038/s41586-018-0476-5.
Seto, K.C., Fragkias, M., 2007. Mangrove conversion and aquaculture development in Vietnam: a remote sensing-based approach for evaluating the Ramsar Convention on Wetlands. Glob. Environ. Chang. 17, 486–500.
Small, C., Nicholls, R.J., 2003. A global analysis of human settlement in coastal zones. J. Coast. Res. 584–599.
Sun, C., Liu, Y., Zhao, S., Li, H., Sun, J., 2017. Saltmarshes response to human activities on a prograding coast revealed by a dual-scale time-series strategy. Estuaries Coasts. https://doi.org/10.1007/s12237-016-0157-2.
Sun, C., Li, J., Liu, Y., Liu, Y., Liu, R., 2021. Plant species classification in salt marshes using phenological parameters derived from Sentinel-2 pixel-differential time-series. Remote Sens. Environ. 256 https://doi.org/10.1016/j.rse.2021.112320.
Tassi, A., Gil, A., 2020. A low-cost Sentinel-2 data and Rao's Q diversity index-based application for detecting, assessing and monitoring coastal land-cover/land-use changes at high spatial resolution. J. Coast. Res. 95, 1315–1319.
Tian, Y., Jia, M., Wang, Z., Mao, D., Du, B., Wang, C., 2020. Monitoring invasion process of *Spartina alterniflora* by seasonal sentinel-2 imagery and an object-based random forest classification. Remote Sens. https://doi.org/10.3390/RS12091383.
Traganos, D., Poursanidis, D., Aggarwal, B., Chrysoulakis, N., Reinartz, P., 2018. Estimating satellite-derived bathymetry (SDB) with the Google Earth Engine and sentinel-2. Remote Sens. https://doi.org/10.3390/rs10060859.
Veloso, A., Mermoz, S., Bouvet, A., Le Toan, T., Planells, M., Dejoux, J.F., Ceschia, E., 2017. Understanding the temporal behavior of crops using Sentinel-1 and Sentinel-2-like data for agricultural applications. Remote Sens. Environ. https://doi.org/10.1016/j.rse.2017.07.015.

Wang, Y., Liu, Y., Jin, S., Sun, C., Wei, X., 2019. Evolution of the topography of tidal flats and sandbanks along the Jiangsu coast from 1973 to 2016 observed from satellites. ISPRS J. Photogramm. Remote Sens. https://doi.org/10.1016/j.isprsjprs.2019.02.001.

Wang, X., Xiao, X., Zou, Z., Chen, B., Ma, J., Dong, J., Doughty, R.B., Zhong, Q., Qin, Y., Dai, S., Li, X., Zhao, B., Li, B., 2020a. Tracking annual changes of coastal tidal flats in China during 1986–2016 through analyses of Landsat images with Google Earth Engine. Remote Sens. Environ. doi: 10.1016/j.rse.2018.11.030.

Wang, X., Xiao, X., Zou, Z., Dong, J., Qin, Y., Doughty, R.B., Menarguez, M.A., Chen, B., Wang, J., Ye, H., Ma, J., Zhong, Q., Zhao, B., Li, B., 2020b. Gainers and losers of surface and terrestrial water resources in China during 1989–2016. Nat. Commun. doi: 10.1038/s41467-020-17103-w.

Wang, X., Xiao, X., Zou, Z., Hou, L., Qin, Y., Dong, J., Doughty, R.B., Chen, B., Zhang, X., Chen, Y., Ma, J., Zhao, B., Li, B., 2020c. Mapping coastal wetlands of China using time series Landsat images in 2018 and Google Earth Engine. ISPRS J. Photogramm. Remote Sens. doi: 10.1016/j.isprsjprs.2020.03.014.

Wang, X., Xiao, X., Xu, X., Zou, Z., Chen, B., Qin, Y., Zhang, X., Dong, J., Liu, D., Pan, L., 2021. Rebound in China's coastal wetlands following conservation and restoration. Nat. Sustain. 4, 1076–1083.

Xiao, X., Boles, S., Liu, J., Zhuang, D., Frolking, S., Li, C., Salas, W., Moore, B., 2005. Mapping paddy rice agriculture in southern China using multi-temporal MODIS images. Remote Sens. Environ. https://doi.org/10.1016/j.rse.2004.12.009.

Xiao, X., Biradar, C.M., Czarnecki, C., Alabi, T., Keller, M., 2009. A simple algorithm for large-scale mapping of evergreen forests in tropical America, Africa and Asia. Remote Sens. https://doi.org/10.3390/rs1030355.

Xiao, X., Dorovskoy, P., Biradar, C., Bridge, E., 2011. A library of georeferenced photos from the field. Eos (Washington. DC). https://doi.org/10.1029/2011EO490002.

Xiao, X., Zhang, Q., Braswell, B., Urbanski, S., Boles, S., Wofsy, S., Moore, B., Ojima, D., 2004. Modeling gross primary production of temperate deciduous broadleaf forest using satellite images and climate data. Remote Sens. Environ. https://doi.org/10.1016/j.rse.2004.03.010.

Xu, H., 2006. Modification of normalised difference water index (NDWI) to enhance open water features in remotely sensed imagery. Int. J. Remote Sens. https://doi.org/10.1080/01431160600589179.

Yim, J., Kwon, B.O., Nam, J., Hwang, J.H., Choi, K., Khim, J.S., 2018. Analysis of forty years long changes in coastal land use and land cover of the Yellow Sea: the gains or losses in ecosystem services. Environ. Pollut. https://doi.org/10.1016/j.envpol.2018.05.058.

Zhang, K., Dong, X., Liu, Z., Gao, W., Hu, Z., Wu, G., 2019. Mapping tidal flats with landsat 8 images and google Earth Engine: a case study of the China's Eastern coastal zone circa 2015. Remote Sens. https://doi.org/10.3390/rs11080959.

Zhang, X., Xiao, X., Wang, X., Xu, X., Chen, B., Wang, J., Ma, J., Zhao, B., Li, B., 2020. Quantifying expansion and removal of Spartina alterniflora on Chongming island, China, using time series Landsat images during 1995–2018. Remote Sens. Environ. https://doi.org/10.1016/j.rse.2020.111916.

Zhu, X., Meng, L., Zhang, Y., Weng, Q., Morris, J., 2019. Tidal and meteorological influences on the growth of invasive *Spartina alterniflora*: evidence from UAV remote sensing. Remote Sens. https://doi.org/10.3390/rs11101208.

Zhu, Z., Woodcock, C.E., 2014. Continuous change detection and classification of land cover using all available Landsat data. Remote Sens. Environ. https://doi.org/10.1016/j.rse.2014.01.011.

Zou, Z., Dong, J., Menarguez, M.A., Xiao, X., Qin, Y., Doughty, R.B., Hooker, K.V., David Hambright, K., 2017. Continued decrease of open surface water body area in Oklahoma during 1984–2015. Sci. Total Environ. https://doi.org/10.1016/j.scitotenv.2017.03.259.